J. Fluid Mech. (1990), *vol.* 221, *pp.* 453–483
Printed in Great Britain

Supersonic gas–particle two-phase flow around a sphere

By R. ISHII,[1] N. HATTA,[2] Y. UMEDA[3] AND M. YUHI[3]

[1] Department of Aeronautics, Kyoto University, Kyoto 606, Japan
[2] Department of Mineral Science and Technology, Kyoto University, Kyoto 606, Japan
[3] Department of Aeronautics, Kyoto University, Kyoto 606, Japan

(Received 19 May 1989 and in revised form 8 May 1990)

This paper describes supersonic flows of a gas–particle mixture around a sphere. The Euler equations for a gas-phase interacting with a particle one are solved by using a TVD (Total Variation Diminishing) scheme developed by Chakravarthy & Osher, and the particle phase is solved by applying a discrete particle-cloud model. First, steady two-phase flows with a finite loading ratio are simulated. By comparing in detail the dusty results with the dust-free ones, the effects of the presence of particles on the flow field in the shock layer are clarified. Also an attempt to correlate the particle behaviours is made with universal parameters such as the Stokes number and the particle loading ratio. Next, non-steady two-phase flows are treated. Impingement of a large particle-cloud on a shock layer of a dust-free gas in front of a sphere is numerically simulated. The effect of particles rebounded from the sphere is taken into account. It is shown that a temporal reverse flow region of the gas is induced near the body axis in the shock layer, which is responsible for the appearance of the gas flow region where the pressure gradient becomes negative along the body surface. These phenomena are consistent with the previous experimental observations. It will be shown that the present results support a flow model for the particle-induced flow field postulated in connection with 'heating augmentation' found in the heat transfer measurement in hypersonic particle erosion environments. The particle behaviour in such flows is so complicated that it is almost impossible to treat the particle phase as an ordinary continuum medium.

1. Introduction

Supersonic two-phase flow over blunt bodies is a very complex engineering and theoretical problem. In reality, it is much more difficult to solve the equations of flow of two-phase media than to solve the equations of ordinary gasdynamics. In this paper we present certain numerical solutions to the problem of a supersonic flow of gas conveying solid particles around a sphere. It is assumed that the particle-phase is dilute and the volume fraction of the particles is negligibly small (Ishii, Umeda & Yuhi 1989).

There have been many studies treating gas–particle flows over blunt bodies. Some important general features of the particle-phase flow in a subsonic or incompressible carrier gas around bodies have previously been made clear. A general discussion on the particle behaviour in a flow field of carrier gas was given in detail by Robinson (1956). At least in cases of negligibly small mass loading ratio of the particles, there can be a tendency for particles to pile up as they move along streamlines in a potential gas flow. In a conserved system, the fact that the particle density increases

along particle streamlines must be compensated for by the creation of dust-free regions. For example, Michael (1968) and Fenández de la Mora & Rosner (1982) showed that a sphere can concentrate a large amount of dust along the limiting particle streamlines which divide the dusty and dust-free regions for particles whose sizes are near the critical one for impaction onset. The possibility of aerodynamic focusing of particles in a carrier gas was investigated by Fernández de la Mora & Riesco-Chueca (1988) in detail.

When the flow field of a carrier gas is rotational, the situation becomes much more complicated. As was discussed by Fernández de la Mora & Riesco-Chueca (1988), the vorticity of the carrier gas has a tendency for the particles to disperse as they move along streamlines. Chung & Troutt (1988) have simulated the behaviour of particle dispersion in an axisymmetric jet, where the large organized structures (vortices) of the carrier gas have played a decisive role in the strong particle dispersion. Under some conditions, particles are flung outside the fluid mixing region of the jet.

In these studies, it is interesting that both the particle focusing in a gas flow around a body and the optimal dispersion of particles in the turbulent mixing layer of a free jet have been correlated successfully with the universal parameter called Stokes number Ψ. This is the product of the relaxation time of the particles and a characteristic value of the velocity gradient in the suspending gas.

In general, theoretically and practically, both particle focusing and particle dispersion, which are obviously antipodal to each other in their physical features, should be expected to occur simultaneously in a carrier gas flow. When the mass loading ratio ν is not negligible but finite, these two opposite tendencies of particles will introduce serious difficulties into the theoretical approach. Disintegration of a large particle cloud into small subclouds may happen in some flow regions and also coalescence or intersection of small subclouds may occur in different flow regions. In such situations, it will be almost impossible to treat the particle phase as an ordinary continuum medium.

For sufficiently dilute particles, aside from particle–particle collisions, their motions are random only because of Brownian motion in a gas, for which the particles are in general too large and heavy, or because of random initial conditions, which would be damped in the early stage of the flow history. Since the gas–particle interactions can effectively suppress the velocity difference among the particles in each local flow region, the possibility of the inter-particle collisions will also be negligibly small unless there are strong fluctuations of the gas flow or there are some fluctuating external forces on the particles. Therefore, in many cases, we may expect the velocity, temperature and density of the particle cloud to vary over a lengthscale of the same order as that of the gas. Because of the absence of randomness in local particle motion, 'the particle pressure' does not appear in the governing equations. Under such a circumstance, the so-called 'two-fluid model' is simplified to a significant degree (Marble 1970).

Generally and strictly speaking, for ordinary suspensions, the velocity, temperature and density of the gas and particles are some statistical properties or some mean (ensemble average or space average) values (Batchelor 1988). Therefore, for instance, the particle velocity is composed of a mean velocity V_p and a fluctuation ΔV_p about that mean with statistical properties such as $\langle \Delta V_p^2 \rangle$, where the angle bracket denotes the mean value. (Here for simplicity, one-dimensional flow is considered.) The random velocity fluctuations might arise from variations in the configuration of particles and resulting hydrodynamic interactions, or, from turbulence in the case of high-Reynolds-number flow even under the condition where

the Brownian motion can be neglected. In the present paper, it will be implicitly assumed that the $\langle \Delta V_p^2 \rangle^{\frac{1}{2}}$ is negligibly small compared with V_p. As pointed out by Batchelor (1989), the tractability of the equations for (laminar) dusty-gas flow is just a consequence of the absence of fluctuations in the particle velocity.

We should like to stress that even in the simplified two-fluid model, the particle phase as well as the gas one can be treated as a continuum medium. There are, however, problems in which the distortion of the particle flow field due to solid walls or due to strong gas flow fluctuations is the central physical issue. For example, when the particles are reflected from the body surface, the reflected particles must be treated as still another component of the mixture, as far as the ordinary continuum model is applied. (If one treats such a flow with a continuum model, the evaluation of mean quantities such as the particle velocity and temperature will become very complicated and also the fluctuations about the means cannot be neglected.) The solution to the problem of flow of a three-phase mixture will be very complex (Matveyef & Seyukova 1981). For a gas–particle flow where the disintegration of particle clouds and/or coalescence or intersection of particle clouds occur, we must treat the flow as a multi-phase flow. Such a flow will be very difficult to solve.

In view of this, Ishii *et al.* (1989) proposed a discrete particle-cloud model for the particle phase. In this model, a whole particle cloud is divided into a large number of small subclouds. In each cloud, the particles have approximately the same velocity and temperature. The particle flow field is obtained by following these individual clouds separately in the whole flow domain. This model can be applied successfully to the problems where multivalue regions for the particle phase appear in the flow field.

In the present paper, steady supersonic flows of gas–particle mixtures over a sphere are solved. First the particle behaviour in a rotational gas flow for $\nu \to 0$ is investigated in detail. Emphasis is placed on the particle impaction and the particle focusing. Next the steady supersonic two-phase flows are solved for a finite loading ratio. By comparing the dust-free and dusty results, effects of the presence of particles on the shock layer and also those of the particle mass loading ratio on the particle impaction are discussed.

Finally, unsteady flows produced by the impinging of a large particle cloud on a shock layer formed in front of a sphere are simulated. Unsteady shock distortion induced by the particles reflected from the body surface is investigated. By comparing the results so obtained with the previous experiments, it will be shown that the numerical results strongly support a flow model for the particle-induced flow field postulated in connection with 'heating augmentation' observed in the heat transfer measurements in hypersonic particle erosion environments (Dunber, Courtney & McMillen 1975; Fleener & Watson 1973).

All the numerical calculations were performed on the super computer Fujitsu VP-400 in the Data Processing Center of Kyoto University.

2. Basic equations

Following the previous paper (Ishii *et al.* 1989), non-dimensional quantities are introduced as follows,

$$\left.\begin{aligned} t = \frac{\bar{c}_\infty \bar{t}}{\bar{L}}, \quad x = \frac{\bar{x}}{\bar{L}}, \quad y = \frac{\bar{y}}{\bar{L}}, \quad \rho = \frac{\bar{\rho}}{\bar{\rho}_\infty}, \quad p = \frac{\bar{p}}{\bar{p}_\infty}, \\ u = \frac{\bar{u}}{\bar{c}_\infty}, \quad v = \frac{\bar{v}}{\bar{c}_\infty}, \quad T = \frac{\bar{T}}{\bar{T}_\infty}, \\ x_\mathrm{p} = \frac{\bar{x}_\mathrm{p}}{\bar{L}}, \quad y_\mathrm{p} = \frac{\bar{y}_\mathrm{p}}{\bar{L}}, \quad u_\mathrm{p} = \frac{\bar{u}_\mathrm{p}}{\bar{c}_\infty}, \quad v_\mathrm{p} = \frac{\bar{v}_\mathrm{p}}{\bar{c}_\infty}, \quad T_\mathrm{p} = \frac{\bar{T}_\mathrm{p}}{\bar{T}_\infty}, \end{aligned}\right\} \tag{1}$$

and

$$f_\mathrm{p} = \frac{C_\mathrm{D}}{C_\mathrm{DS}}, \quad g_\mathrm{p} = \frac{Nu}{Nu_\mathrm{S}}, \tag{2}$$

$$\Gamma_\tau = \frac{\bar{\tau}_\mathrm{A}}{\bar{\tau}_\mathrm{F}}, \quad \Gamma_\rho = \frac{\bar{\rho}_\mathrm{mp}}{\bar{\rho}_\infty}, \tag{3}$$

$$\nu_\infty = \frac{\bar{\rho}_{\mathrm{p}\infty}}{\bar{\rho}_\infty}, \quad \gamma = \frac{\bar{C}_{pg}}{\bar{C}_{vg}}, \quad \theta = \frac{\bar{C}_{pp}}{\bar{C}_{pg}}, \tag{4}$$

where t, x, y are the time, axial distance and radial distance, respectively; ρ, u, v, p, T and c are the density, the axial velocity, radial velocity, pressure, temperature and speed of sound of the gas, respectively. $\bar{L}$ is a reference length of the flow field and here the sphere radius is taken as $\bar{L}$. The subscripts p and ∞ denote particles and uniform flow conditions, respectively, and overbars denote the dimensional quantities. The location of a particle at a time t is denoted by $(x_\mathrm{p}, y_\mathrm{p})$. $\bar{C}_{vg}$ and $\bar{C}_{pg}$ are the specific heats at constant volume and pressure of the gas, $\bar{C}_{pp}$ is the specific heat of the particle material, γ is the ratio of specific heats of the gas, C_D is the particle drag coefficient, Nu is the Nusselt number and $\bar{\rho}_\mathrm{mp}$ is the material density of the particles. The subscript S denotes the Stokes flow regime.

The non-dimensional parameter Γ_τ is defined as a ratio of the aerodynamic response time of a particle assuming the Stokes drag law, $\bar{\tau}_\mathrm{A}$, to a characteristic time of the flow field, $\bar{\tau}_\mathrm{F}$. These are expressed as

$$\bar{\tau}_\mathrm{A} = \frac{\bar{\rho}_\mathrm{mp}(2\bar{r}_\mathrm{p})^2}{18\bar{\mu}}, \quad \bar{\tau}_\mathrm{F} = \frac{\bar{L}}{\bar{c}_\infty}. \tag{5}$$

Here $\bar{\mu}$ is the gas viscosity given by

$$\bar{\mu} = \bar{\mu}_\infty \left(\frac{\bar{T}}{\bar{T}_\infty}\right)^\delta, \tag{6}$$

where δ is an appropriate constant. The parameters f_p and g_p are the modifying factors of the drag coefficient and the Nusselt number, respectively. C_D and Nu used in the present study are those given by Henderson (1976) and Carlson & Hoglund (1973), respectively.

By applying the discrete particle-cloud model and introducing suitable assumptions, the basic equations for the present axisymmetric system are given in terms of these non-dimensional quantities in the following sections.

2.1. *Particle phase*

By labelling the particles by subscripts i ($i = 1, 2, 3, \ldots$) and denoting their locations by $(x_{\mathrm{p}i}(t), y_{\mathrm{p}i}(t))$, the particle motion obeying Newton's law is described by

$$\frac{\mathrm{d}U_{\mathrm{p}i}}{\mathrm{d}t} = I_{\mathrm{p}i}, \tag{7}$$

where
$$U_{\mathrm{p}}=\begin{bmatrix} x_{\mathrm{p}} \\ y_{\mathrm{p}} \\ u_{\mathrm{p}} \\ v_{\mathrm{p}} \\ T_{\mathrm{p}} \end{bmatrix}, \quad I_{\mathrm{p}}=\begin{bmatrix} u_{\mathrm{p}} \\ v_{\mathrm{p}} \\ A_{\mathrm{p}}(u-u_{\mathrm{p}}) \\ A_{\mathrm{p}}(v-v_{\mathrm{p}}) \\ B_{\mathrm{p}}(\mathrm{T}-\mathrm{T}_{\mathrm{p}}) \end{bmatrix}. \tag{8}$$

The parameters A_{p} and B_{p} are defined by

$$A_{\mathrm{p}}=\frac{f_{\mathrm{p}}}{\Gamma_{\tau}}, \quad B_{\mathrm{p}}=\frac{2g_{\mathrm{p}}}{3Pr\theta\Gamma_{\tau}}, \tag{9}$$

where Pr is the Prandtl number of the gas.

2.2. *Gas phase*

The governing equations for the gas-phase are written in the cylindrical coordinate system as

$$\frac{\partial U}{\partial t}+\frac{\partial F}{\partial x}+\frac{\partial G}{\partial y}+H+H_{\mathrm{p}}=0, \tag{10}$$

where

$$\left.\begin{aligned} U&=\begin{bmatrix} \rho \\ \rho u \\ \rho v \\ e \end{bmatrix}, \quad F=\begin{bmatrix} \rho u \\ \rho u^2+p/\gamma \\ \rho uv \\ u(e+p/\gamma) \end{bmatrix}, \quad G=\begin{bmatrix} \rho v \\ \rho uv \\ \rho v^2+p/\gamma \\ v(e+p/\gamma) \end{bmatrix}, \\ H&=\frac{1}{y}\begin{bmatrix} \rho v \\ \rho uv \\ \rho v^2 \\ v(e+p/\gamma) \end{bmatrix}, \quad H_{\mathrm{p}}=\begin{bmatrix} 0 \\ F_{\mathrm{p}x} \\ F_{\mathrm{p}y} \\ W_{\mathrm{p}} \end{bmatrix}, \\ F_{\mathrm{p}x}&=\nu_{\infty}\left(\frac{1}{S_{\mathrm{p}}}\right)\sum N_{\mathrm{p}k}A_{\mathrm{p}k}(u-u_{\mathrm{p}k}), \\ F_{\mathrm{p}y}&=\nu_{\infty}\left(\frac{1}{S_{\mathrm{p}}}\right)\sum N_{\mathrm{p}k}A_{\mathrm{p}k}(v-v_{\mathrm{p}k}), \\ W_{\mathrm{p}}&=uF_{\mathrm{p}x}+vF_{\mathrm{p}y}-\nu_{\infty}\left(\frac{1}{S_{\mathrm{p}}}\right)\sum N_{\mathrm{p}k}\left\{A_{\mathrm{p}k}[(u-u_{\mathrm{p}k})^2+(v-v_{\mathrm{p}k})^2]\right. \\ &\quad\left.-\frac{\theta}{(\gamma-1)}B_{\mathrm{p}k}(T-T_{\mathrm{p}k})\right\}, \\ N_{\mathrm{p}k}&=\left(\frac{y^*_{\mathrm{p}k}}{y_{\mathrm{p}k}}\right)N^*_{\mathrm{p}k}, \end{aligned}\right\} \tag{11}$$

where $y^*_{\mathrm{p}k}$ and $N^*_{\mathrm{p}k}$ are the radial coordinate of a particle located at the centre of a k-cloud injected into the flow field and the number of particles contained per unit length of the cloud, and S_{p} is a suitable averaging domain. The above system is supplemented by

$$e=\frac{p}{\gamma(\gamma-1)}+\tfrac{1}{2}\rho(u^2+v^2), \tag{12}$$

$$p=\rho T, \tag{13}$$

$$c^2=T. \tag{14}$$

3. Numerical procedure

For an effective solution of the gas-phase flow, the physical space (x, y) is transformed into a computational one (ξ, η) by

$$\xi = (x^2+y^2)^{\frac{1}{2}}, \quad \eta = \tan^{-1}(y/x), \tag{15}$$

herewith, the governing equation (10) is rewritten as

$$\frac{\partial \tilde{U}}{\partial t}+\frac{\partial \tilde{F}}{\partial \xi}+\frac{\partial \tilde{G}}{\partial \eta}+\tilde{H}+\tilde{H}_{\mathrm{p}} = 0, \tag{16}$$

where

$$\left.\begin{aligned} \tilde{U} &= \frac{U}{J}, \\ \tilde{F} &= \frac{1}{J}(\xi_x F+\xi_y G), \quad \tilde{G} = \frac{1}{J}(\eta_x F+\eta_y G), \\ \tilde{H} &= \frac{H}{J}, \quad \tilde{H}_{\mathrm{p}} = \frac{H_{\mathrm{p}}}{J}. \end{aligned}\right\} \tag{17}$$

Here J is a Jacobian of the transformation defined as

$$J = \frac{\partial(\xi, \eta)}{\partial(x, y)} = \xi_x \eta_y - \xi_y \eta_x. \tag{18}$$

The physical domain considered here and the transformed computational one are shown in figure 1. The calculation domain is the region surrounded by the axis AB, the outer boundary BC, the downstream boundary CD and the sphere surface DA. The number of the mesh is 100×100 and that of the subclouds of particles is 1000×300 for the two-phase solutions.

In the present calculations, the gas-phase flow is solved in the computational space (ξ, η) and the particle-phase is solved directly in the physical space (x, y). Of course, it is quite possible to formulate the basic equations in the spherical coordinate system (ξ, η) from the beginning, and also the present calculation can be performed in this coordinate system for both the gas and the particle phases.

From the numerical point of view, however, the spherical coordinate system has not enough flexibility for the flow geometry to be treated and so is not convenient for general use. The numerical scheme used here is, therefore, first constructed in the cylindrical coordinate system (x, y) and then is transformed into that in the spherical coordinate system described above. For the particle phase, there is no difficulty in solving the system in the (x, y)-space and also the governing equations are much simpler in the (x, y)-space than in the (ξ, η)-space.

The numerical procedure is essentially the same as that in the previous paper (Ishii *et al.* 1989). First the time interval Δt is determined by the CFL (Coulant–Friedrichs–Lewy) condition for the gas-phase flow (Godunov 1959) and this Δt is also used in the particle-phase solution. Although it is not always accepted that such a treatment is justified, it was confirmed that in these calculations Δt determined by the CFL condition was always much smaller than the particle relaxation times t_{pV} and t_{pT} for the present flow conditions. In a few cases, it was also found that the numerical results for a flow were not appreciably changed by adopting different time intervals such as Δt and $\frac{1}{2}\Delta t$, where Δt is a standard time interval employed here.

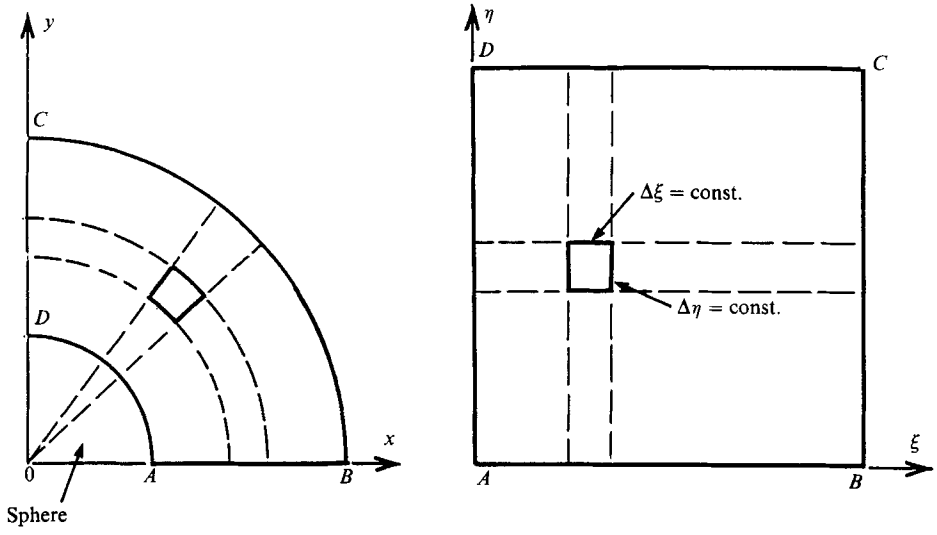

FIGURE 1. Calculation domain. The domain $ABCDA$ in the (x, y)-plane is transformed into a rectangular domain $ABCDA$ in the (ξ, η)-plane.

The boundary conditions applied here are as follows: the symmetry condition is applied on the boundaries AB and DA, the uniform flow condition on the outer boundary BC and the outflow condition on CD (Matsuda *et al.* 1987).

As the initial flow condition, a uniform gas at rest at $p = 1$ and $\rho = 1$ is assumed to occupy the whole computational domain and a rigid sphere is placed in it. At $t = 0$, a uniform supersonic flow begins to enter the computational domain through the boundary BC. Since a time-dependent technique is applied, the steady flow is obtained as a time-converged solution. The time-converged one-phase solution is employed for the calculations of two-phase flows with a finite loading ratio as an initial flow condition.

4. Numerical results

The Euler solver used in the present study is the TVD-scheme developed by Chacravarthy & Osher (1985), which can be third-order accurate in space and second-order accurate in time. The number density of particle clouds considered here is about 1.5 times larger than that in the previous case (Ishii *et al.* 1989). The CFL number was taken to be 0.5 for all the calculations.

The physical constants for the gas as well as the particles used here are listed in table 1.

4.1. *Preliminary check of numerical scheme*

Although the purpose of this paper is to investigate two-phase flows, it will be worth giving a brief description of dust-free (one-phase) solutions. This is also necessary for a preliminary check of the validity and reliability of the present numerical scheme.

The solutions for various Mach numbers M_∞ have demonstrated a satisfactory time-convergence of the flow field. The profiles of the pressure distribution along the sphere surface were compared with the theoretical results given by Belotserkovskii (1960), which have been proved to agree well with the experiments, and the pressures and densities just behind the bow shock and at the stagnation point on the body axis were compared with the exact values. In these comparisons, excellent agreement was

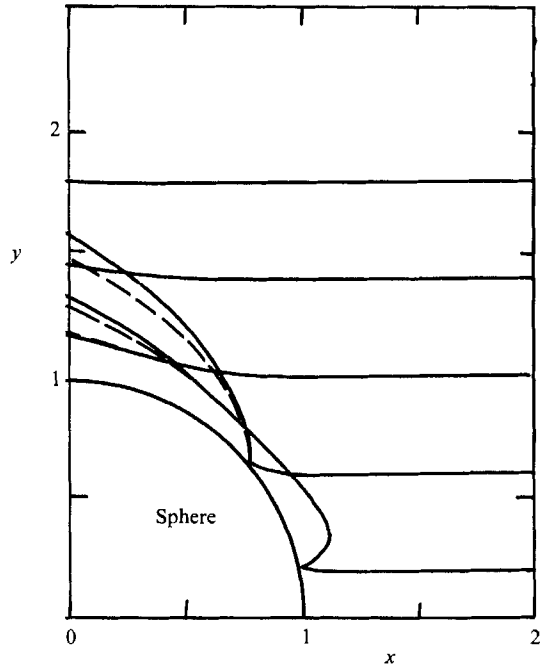

FIGURE 2. Comparison between particle streamlines in a supersonic gas flow for different particle drag coefficients, $M_\infty = 3$, $\bar{p}_\infty = 0.1$ atm, $\bar{T}_\infty = 290$ K, $\bar{L} = 3$ cm, $\bar{r}_p = 1$ μm, $\Psi_r = 4.4$; ——, Henderson; – – –, Gilbert *et al.*

Gas (air)	Particles (Al_2O_3)
$\gamma = 1.4$	$\bar{\rho}_{mp} = 4.0 \times 10^3$ kg/m^3
$\bar{C}_{pg} = 1005$ J/kg K	$\bar{C}_{pp} = 1686$ J/kg K
$\bar{\mu} = 1.79 \times 10^{-5}$ kg/m s (for $\bar{T} = 288$ K)	
$\delta = 0.5$	
$P_r = 0.75$	

TABLE 1. Physical constants of gas and particles

obtained. It was also confirmed that the shock stand-off distances agree very well with the previous experiments and theories (Van Dyke 1958).

4.2. *Particle trajectories in a carrier gas*

In various industrial fields, it is often crucially important to know the particle trajectories in a carrier gas. In this section, the motion of particles in the gas flow obtained in the previous section is investigated in detail. Since the presence of particles does not affect the gas-phase flow in the limit where $\nu \to 0$, the particle motion can be determined for a fixed flow field of the gas. The particles are injected into the flow field at various locations on a plane perpendicular to the body axis ahead of the bow shock. It is assumed that the particles have the same velocities and temperatures as those of the gas at the injection points.

Figure 2 shows the particle streamlines for $\bar{r}_p = 1$ μm. In order to confirm the generality of the present results, the particle streamlines were calculated by using two different particle drag coefficients C_D; one of which is given by Henderson (1976) and the other by Gilbert, Davis & Altman (1955). The former takes account of

rarefaction, inertial and compressibility effects and also that of a temperature difference between the particle and the gas. The latter includes the inertial effect only. Here, it is assumed that the particles which impinge on the body surface are reflected perfectly elastically. The reflection of particles from the sphere makes the residence time of the particles in a shock layer very long, which is helpful for detecting the difference between the two cases. Obviously, the particle streamlines for these drag coefficients are slightly different from each other for particles impinging on the sphere. They deviate appreciably only in the flow region near the downstream boundary, where the rarefaction effect may become important for the drag coefficient. From this, one may conclude that the present numerical results do not depend on the particle drag coefficient, at least for the particle streamlines in the shock layer in front of the sphere. In what follows, all the calculations are carried out by using C_D given by Henderson (1976).

It is generally and reasonably expected that the particle behaviour in a gas flow can be characterized by the Stokes number Ψ defined as

$$\Psi = \left[\frac{\bar{\rho}_{mp}(2\bar{r}_p)^2}{18\bar{\mu}f_p}\right] \Big/ \left[\frac{\bar{L}}{\bar{U}}\right], \tag{19}$$

where $\bar{L}$ and $\bar{U}$ are an appropriate characteristic length and a reference velocity of the gas flow, respectively. Recently, Forney & McGregor (1987) have proposed a modified Stokes number by suitable choice of $\bar{L}$ and $\bar{U}$ as

$$\Psi_r = \frac{4}{3}\left(\frac{\bar{\rho}_{mp}}{\bar{\rho}}\right)\left(\frac{2\bar{r}_p}{\bar{\Delta}}\right)\Phi_c \int_0^{Re_p} \frac{dRe}{C_D Re} \tag{20}$$

where Re_p is the particle Reynolds number given by

$$Re_p = 2\bar{r}_p \bar{\rho} \Delta\bar{u}_p / \bar{\mu}. \tag{21}$$

Here $\Delta\bar{u}_p$ is the particle velocity relative to the gas, and Φ_c is the collection factor due to departure from the continuum flow of the gas around a particle. Equation (20) has been derived by an adaptation of the formula of Israel & Rosner (1983) to the case of supersonic flows. In the evaluation of Ψ_r from (20), the term $\bar{T}/\bar{T}_p$ in C_D is fixed at unity. The shock stand-off distance $\bar{\Delta}$ is taken as the reference length of the flow field.

Figure 3 shows the particle and the gas streamlines for $M_\infty = 3$, $\bar{p}_\infty = 0.5$ atm, $\bar{T}_\infty = 290$ K, $L = 3$ cm and $\bar{r}_p = 0.5$ μm ($\Psi_r = 0.925$). The dotted lines are gas streamlines while solid lines are particle ones. In this figure, strong particle concentration is observed in the region near the grazing point of the particles. But in this case, it was confirmed that the particle focusing (crossing of particle trajectories) is not realized at least within the numerical accuracy.

Although we treat the particle phase partly as a discrete one in the present numerical analysis, at least for theoretical discussion it is sometimes very helpful to consider an analogy between the ideal gas and the particle phase. For example, Morioka & Nakajima (1987) proposed a flow model for the particle phase, where the particles are taken to be large and heavy molecules and a linearized Boltzmann equation is applied to them. By using a Chapman–Enskog expansion technique, they derived conservation equations for the particle phase. It must be noticed that in their model the usual 'particle temperature T_p' is treated as an internal energy and then it is not related to the random motion of the particles, and also the interactions between the gas and the particle phases are taken into account by introducing some external force and energy source terms corresponding to the interactions.

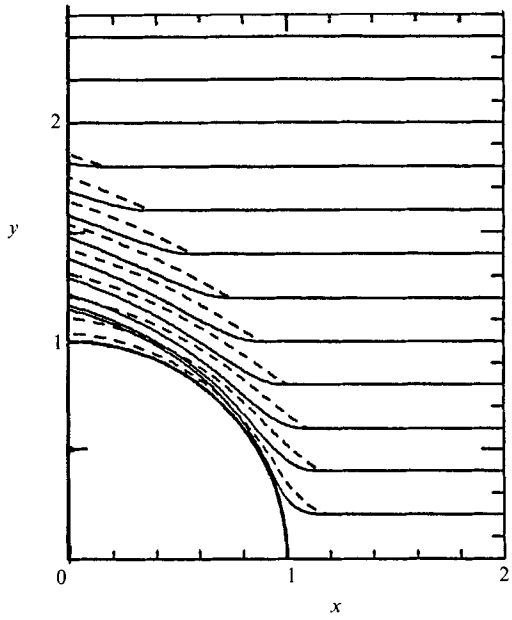

FIGURE 3. Gas and particle streamlines, $M_\infty = 3$, $p_\infty = 0.5$ atm, $\bar{T}_\infty = 290$ K, $\bar{L} = 3$ cm, $\bar{r}_p = 0.5$ μm, $\Psi_r = 0.925$; ---, gas; ——, particles.

According to this theory, 'the speed of sound' in the particle phase c_p may be defined by

$$c_p = \text{const} \times T_{ptr}^{\frac{1}{2}}, \tag{22}$$

owing to the analogy with the kinetic theory, where T_{ptr} is a 'particle translational temperature' ($T_{ptr} \neq T_p$). Under the condition that the velocity fluctuation of the particles is negligible, it follows that

$$T_{ptr} \to 0, \quad M_p = V_p/c_p \to \infty, \tag{23}$$

where V_p and M_p are the velocity and the Mach number of the particle phase, respectively.

It is important to realize that the fluctuation of the particle velocity in this theory does not directly relate to the random motion of the gas molecules. Actually in a gas–particle mixture, gas molecules are always colliding at random with particles and then even the heavy particles will have some random motion owing to the randomness of the thermal velocity of the gas molecules. Since, however, the ratio of the mass of a gas molecule to that of a particle is negligibly small, such a random motion of the particles can be neglected without loss of reasonableness and generality in the fluid dynamics and thermodynamics of the gas–particle mixture.† The randomness of the particle motion is then essentially different from that of thermal motion of the gas molecules in the kinetic theory. In cases where the direct interaction between the particles is negligible, the random motion of the particles can be produced only through interactions with the local fluctuations of the gas phase flow, which are not microscopic but just macroscopic in the gasdynamic sense. One cannot get any information on the random motion of the particles from the thermal motion of the molecules.

† The particles in the dusty-gas theory should have some bulk properties such as the material density and specific heat and the surface tension. For example, it is said that at least one thousand H_2O molecules are necessary for a small droplet of water to possess its normal surface-tension value.

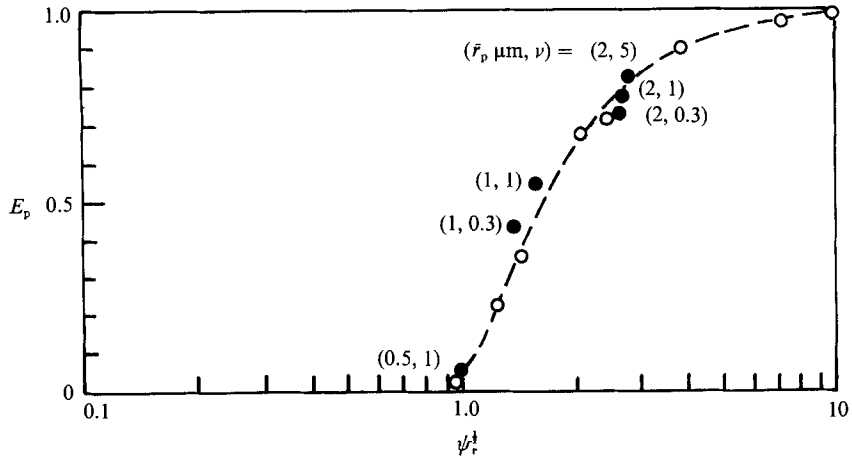

FIGURE 4. Collection factors E_p against the modified Stokes number Ψ_r. ●, results for $\nu_\infty > 0$, $M_\infty = 3$, $\bar{p}_\infty = 0.5$ atm, $\bar{T}_\infty = 290$ K, $\bar{L} = 3$ cm; ○, results for $\nu_\infty \to 0$. ---, curve which fits to the numerical results for $\nu_\infty \to 0$.

The present definition of the 'sound velocity of the particle phase' and then that of the 'particle translational temperature' might not be physically appropriate when the inter-particle collision is negligible. In this sense, as was discussed previously, (23) should be replaced by

$$\langle \Delta V_p^2 \rangle^{\frac{1}{2}} \to 0, \quad M_p \sim \frac{V_p}{\langle \Delta V_p^2 \rangle^{\frac{1}{2}}} \to \infty. \tag{24}$$

In gasdynamics, one of the most important features of subsonic motion is incompressibility, which results from the fact that the molecular motion is fast compared with the mean convective speed. Following this, it will be possible to consider M_p in (24) as a kind of 'Mach number of the dilute particle phase'. (It has to be pointed out that there are some differences between the two-component gas mixture and the two-phase mixture (Lhuillier 1986).)

Thus, the particles can be highly supersonic with respect to their own fluctuation motion, that is, highly compressible (Fernández de la Mora & Riesco-Chueca 1988). Hence the particle-free region as well as the particle concentration can easily be realized in a flow region. In many practical cases, the particle phase flow actually presents such behaviours. Clearly, main features of the present results are quite consistent with these discussions. For example, as shown in figures 11–13, dust-free regions appear and the strong particle concentration is realized near the limiting particle streamlines.

It has been found that the particle concentration is an important feature of the particulate flow especially when the carrier gas is irrotational. On the contrary, however, rotational flows disfavour the particle focusing. Since the gas flow field in the shock layer is rotational, the vorticity in the gas flow field will be against the particle concentration. A typical example of the particle concentration was observed in figure 13. At least for the flow and the particle conditions considered here, it was numerically confirmed that the particle focusing (crossing of particle trajectories) is not realized for any value of Ψ_r.

In practice, much attention has been paid to finding the collection efficiency E_p, which is defined as the ratio of the number of particles impacting with the object to the number of particles which would impinge on it, if they followed straight-line

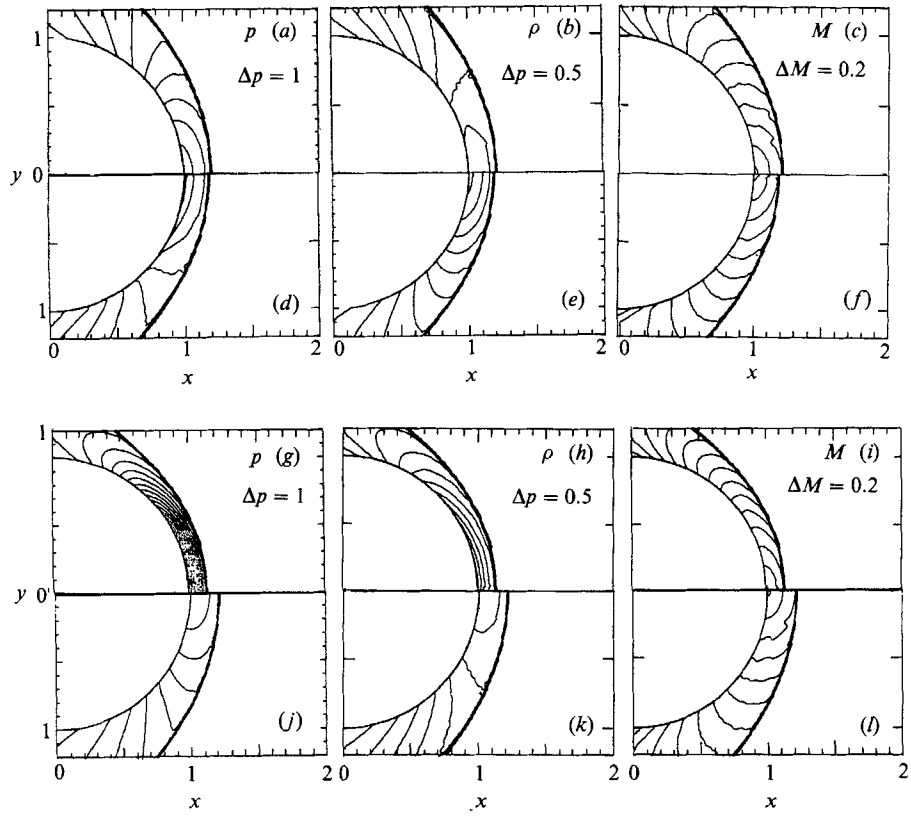

FIGURE 5. Contours of constant pressure, density and temperature, $M_\infty = 3$, $\bar{p}_\infty = 0.5$ atm, $\bar{T}_\infty = 290$ K, $\bar{L} = 3$ cm, $n = 2200$; (*a*), (*b*), (*c*) $\nu_\infty = 0.3$, $\bar{r}_p = 2$ μm, $\Psi_r = 7.21$; (*d*), (*e*), (*f*) $\nu_\infty = 0.3$, $\bar{r}_p = 1$ μm, $\Psi_r = 1.93$; (*g*), (*h*), (*i*) $\nu_\infty = 5.0$, $\bar{r}_p = 2$ μm, $\Psi_r = 7.94$; (*j*), (*k*), (*l*) $\nu_\infty \to 0$.

trajectories without any deflection by the gas. The present results are plotted against the modified Stokes number Ψ_r in figure 4, where the dashed line simply shows a curve fitting to the numerical results for $\nu \to 0$. The present collection factor E_p is clearly correlated fairly well with this parameter Ψ_r.

4.3. *Steady two-phase flows*

In this section, gas–particle two-phase flows with a finite loading ratio are calculated and the effects of the presence of particles on the flow field are investigated. These will also be compared with the unsteady results in the following chapter. Because of limitation of the computer memory, it is assumed that the particles impinging on the body surface are absorbed by the surface (perfectly inelastic collision).

Denoting the height of the plane by R, which is located upstream from the bow shock and at which the particles are injected, the axial and radial widths of the k-particle cloud Δx^*_{pk} and Δy^*_{pk}, respectively, are given by

$$\left.\begin{aligned} \Delta x^*_{pk} &= |u^*|\,\Delta t, \\ \Delta y^*_{pk} &= R/K, \end{aligned}\right\} \tag{25}$$

where K is the number of particle clouds injected into the flow field at each timestep. Here, R and K are set to 1.25 and 300, respectively. Since $|u^*|\,\Delta t$ and R/K are much smaller than the mesh sizes Δx and Δy, the condition that $\Delta x_{pk}\,\Delta y_{pk} \ll S_p (= \Delta x \Delta y)$ is satisfied.

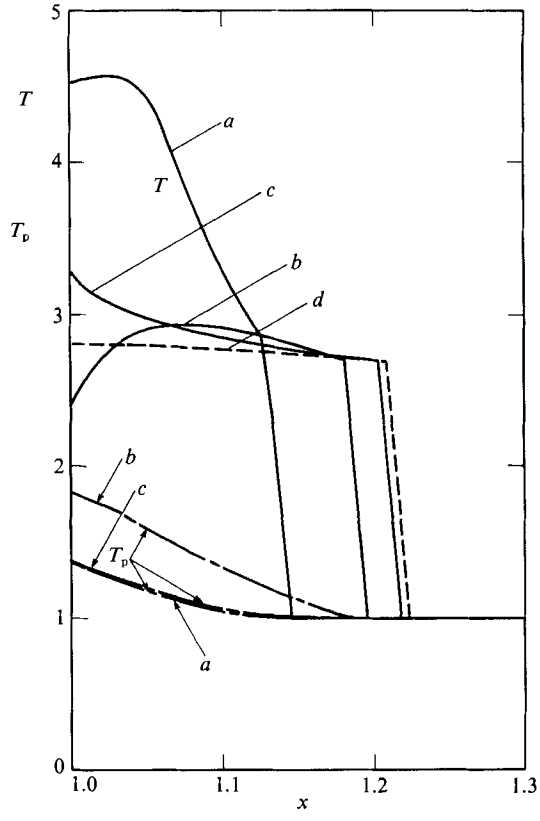

FIGURE 6. Temperature distributions of gas and particles along the body axis, $M_\infty = 3$, $p_\infty = 0.5$ atm, $\bar{T}_\infty = 290$ K, $\bar{L} = 3$ cm, $n = 2200$; *a*. $\bar{r}_p = 2$ μm, $\nu_\infty = 5$, $\Psi_r = 7.94$, *b*. $\bar{r}_p = 1$ μm, $\nu_\infty = 0.3$, $\Psi_r = 1.93$; *c*. $\bar{r}_p = 2$ μm, $\nu_\infty = 0.3$, $\Psi_r = 7.21$; *d*. $\nu_\infty \to 0$.

The steady dust-free result obtained in §4.1 was used as the initial-flow condition. It took more than 1500 timesteps to get a time-converged solution after the injection of particle clouds into the flow field. Here only the time-converged solutions ($n = 2200$) will be presented.

Contours of constant pressure, density and Mach number are shown in figure 5 for dusty flows. It can be seen from them that the main features of the dusty results are essentially the same as those presented in the previous paper (Ishii *et al.* 1989), that is the constant Mach number contours of the dusty gas are rather close to those of the dust-free one, while the contours of constant pressure and density are considerably different from the dust-free case (see figures 5*g*–5*i*). The shock stand-off distance for the two-phase flow is appreciably decreased. This trend becomes stronger with larger loading ratio and smaller particle radius (or smaller modified Stokes number Ψ_r).

For closer investigation of the two-phase shock layer, axial distributions of the temperature, velocity, density and pressure of the gas and the temperature and velocity of the particles are shown in figures 6–9. At first glance, it may be seen that the structure of the dusty shock layer is strongly dependent on the Stokes number Ψ_r and the particle loading ratio ν_∞. The most important effect of these parameters is seen in the temperature distributions of the gas (figure 6).

When the gas passes through the bow shock, its velocity decreases discontinuously in magnitude. On the other hand, the change in the particle velocity is continuous

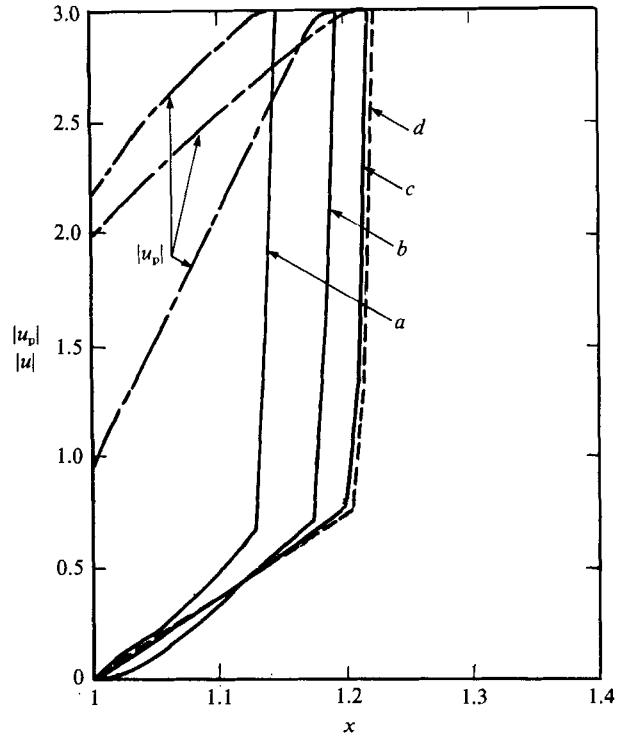

FIGURE 7. Velocity distributions of gas and particles along the body axis, $M_\infty = 3$, $\bar{p}_\infty = 0.5$ atm, $\bar{T}_\infty = 290$ K, $\bar{L} = 3$ cm, $n = 2200$; *a*. $\bar{r}_p = 2$ μm, $\nu_\infty = 5$, $\Psi_r = 7.94$; *b*. $\bar{r}_p = 1$ μm, $\nu_\infty = 0.3$, $\Psi_r = 1.93$; *c*. $\bar{r}_p = 2$ μm, $\nu_\infty = 0.3$, $\Psi_r = 7.21$; *d*. $\nu_\infty \to 0$.

across the bow shock because of the large inertia of the particle. The magnitude of the particle velocity decreases along the stagnation streamline. As a result, the relative velocity between the gas and the particle takes the maximum value just behind the bow shock. Thus, the frictional heat is generated most effectively near the bow shock. This heat is responsible for the steep increase of the gas temperature in the shock layer while this does not occur in the dust-free case. When the Stokes number Ψ_r is close to unity, the relative velocity is appreciably decreased, as the particle approaches the sphere surface, and therefore the heat transferred from the gas to the particles dominates over the heat supply owing to frictional heat-production. It follows that the gas temperature becomes highest at a certain region behind the bow shock and it decreases significantly near the body surface (see the curve for $\Psi_r = 1.93$ in figure 6). For $\Psi_r \gg 1$, since the particles are not effectively decelerated in the shock layer, the highest temperature is realized at the body surface (see the curve for $\Psi_r = 7.21$ in figure 6). This situation is, however, changeable with the loading ratio. In the case of $\nu_\infty = 5$, although the Stokes number is much larger than unity ($\Psi_r = 7.94$), the highest temperature is realized somewhat upstream of the body surface. In this case, the deceleration of the particle velocity is nearly the same as that in the above case. However, the gas temperature is significantly increased owing to the large frictional heat. And then the temperature difference $T - T_p$, to which the heat transfer from the gas to the particles is nearly proportional, becomes very large. Thus, the gas temperature decreases near the body surface for large particle loading ratio (see the curve for $\Psi_r = 7.94$ in figure 8).

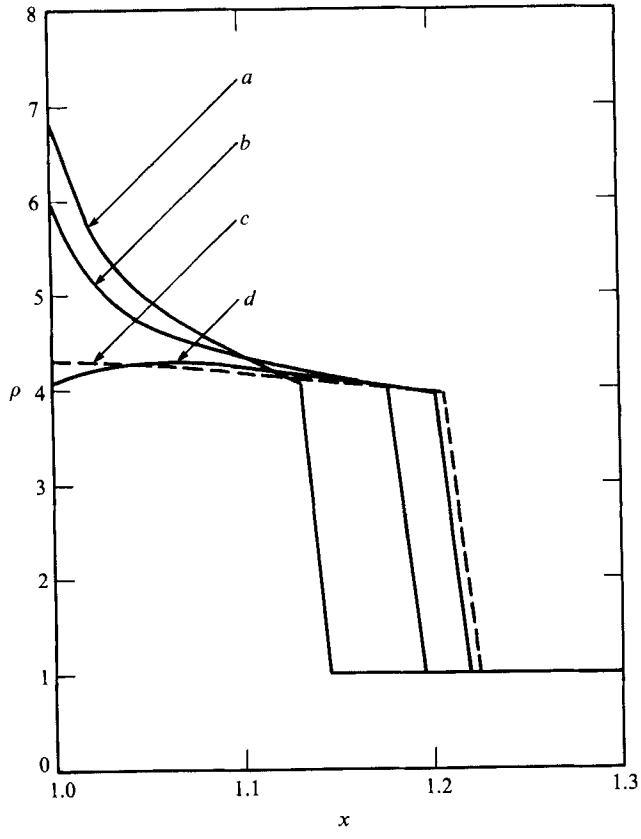

FIGURE 8. Density distribution of gas along the body axis, $M_\infty = 3$, $\bar{p}_\infty = 0.5$ atm, $\bar{T}_\infty = 290$ K, $\bar{L} = 3$ cm, $n = 2200$; *a*. $\bar{r}_p = 2$ μm, $\nu_\infty = 5$, $\Psi_r = 7.94$; *b*. $\bar{r}_p = 1$ μm, $\nu_\infty = 0.3$, $\Psi_r = 1.93$; *c*. $\bar{r}_p = 2$ μm, $\nu_\infty = 0.3$, $\Psi_r = 7.21$; *d*. $\nu_\infty \to 0$.

In figure 7, velocity distributions of the gas for $\nu_\infty = 0.3$, $\bar{r}_p = 1.0$ μm and $\nu_\infty = 5.0$, $\bar{r}_p = 2.0$ μm show a nonlinear behaviour near the stagnation point. This phenomenon corresponds to the structure of each shock layer as shown in figures 6, 8 and 9. In these flows, the gas density increases very steeply and the gas temperature becomes very high near the stagnation region. These will affect the rate of momentum transfer between the gas and the particles in a complicated manner, and will be responsible for the nonlinear behaviour of the gas velocity. It has to be stressed, however, that the two-phase results are not always completely time-converged even for large numbers of the timestep n, owing to the discrete treatment of the particle phase. Some artificial fluctuations of the particle behaviour are inevitably produced numerically. This phenomenon is most prominent near the stagnation region. The gas flow in this region will in turn be fluctuated by the artificial disturbances of the particles. Then the detailed quantitative discussions about local derivatives of the gas velocity near the stagnation region, where the fluctuation of the gas velocity can be the same order with the velocity itself, will not be appropriate.

Obviously the flow behaviour along the axis behind the bow shock is similar to that behind a plane shock wave propagating in a uniform gas–particle mixture (Ishii 1983). For example, the overshooting of the gas temperature and the nonlinear decrease in the gas velocity are found in the latter case, too. The most prominent differences between them are realized in the region near the sphere surface. In the

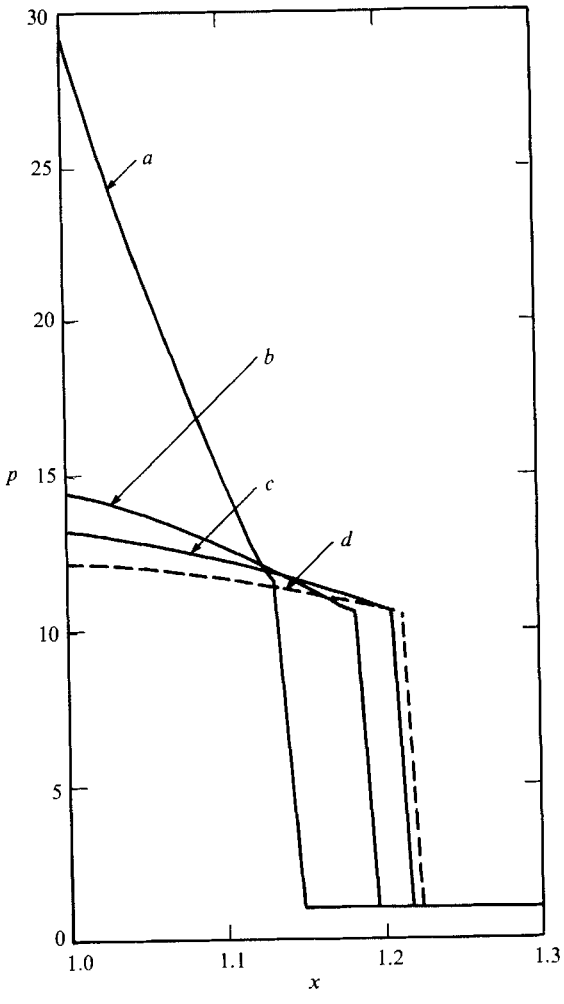

FIGURE 9. Pressure distribution of gas along the body axis, $M_\infty = 3$, $\bar{p}_\infty = 0.5$ atm, $\bar{T}_\infty = 290$ K, $\bar{L} = 3$ cm, $n = 2200$; *a*. $\bar{r}_p = 2$ μm, $\nu_\infty = 5$, $\Psi_r = 7.94$; *b*. $\bar{r}_p = 1$ μm, $\nu_\infty = 0.3$, $\Psi_r = 1.93$; $\bar{r}_p = 2$ μm, $\nu_\infty = 0.3$, $\Psi_r = 7.21$; *d*. $\nu_\infty \to 0$.

present cases, as shown in figures 6–9, all the quantities change most significantly near the stagnation point owing to the presence of the sphere.

The shapes of the bow shock are shown in figure 10. This suggests that the bow shock is dependent on the particle loading ratio ν_∞ as well as the Stokes number Ψ_r. It may be natural and reasonable to conclude that the shock stand-off distance for the dusty flow is always smaller than that for the dust-free flow. The effect of the Stokes number on the bow shock is shown in figure 10(*b*), where the results are for fixed gas conditions and a fixed loading ratio. This figure shows that the shock stand-off distance is a decreasing function of the Stokes number.

For more detailed discussions, it will be instructive and helpful to consider a limiting case of $\Psi_r \to 0$. In this case, we can treat the mixture as a single fluid and can introduce two effective parameters

$$\gamma_e = \frac{\gamma(1+\nu_\infty \theta)}{(1+\gamma\nu_\infty \theta)}, \quad \bar{c}_e^2 = \frac{\gamma_e \bar{R}\bar{T}}{1+\nu_\infty}, \tag{26}$$

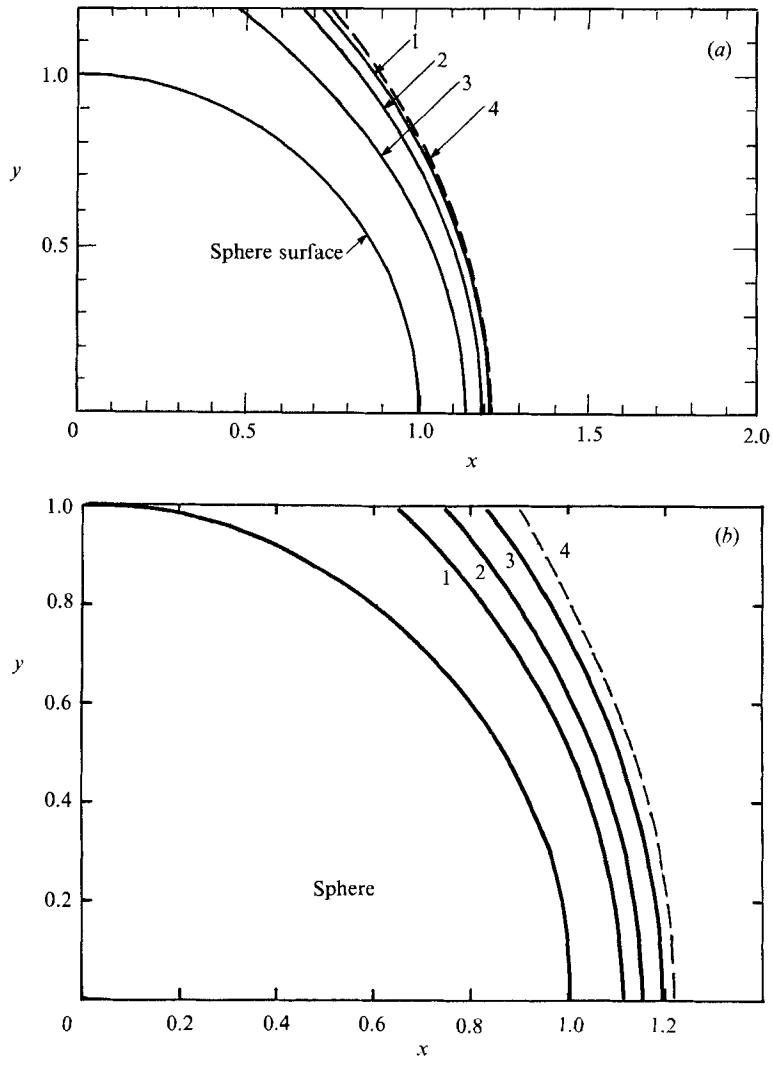

FIGURE 10. Bow shock waves, $M_\infty = 3$, $\bar{p}_\infty = 0.5$ atm, $\bar{T}_\infty = 290$ K, $\bar{L} = 3$ cm, $n = 2200$, (*a*) Effect of particle loading ratio ν_∞; 1. $\bar{r}_p = 2$ μm, $\nu_\infty = 0.3$, $\Psi_r = 7.21$; 2. $\bar{r}_p = 1$ μm, $\nu_\infty = 0.3$, $\Psi_r = 1.93$; 3. $\bar{r}_p = 2$ μm, $\nu_\infty = 5.0$, $\Psi_r = 7.94$; 4. $\nu_\infty \to 0$, (*b*) Effect of Stokes number; 1. $\bar{r}_p = 0.5$ μm, $\nu_\infty = 1.0$, $\Psi_r = 1.01$, 2. $\bar{r}_p = 1$ μm, $\nu_\infty = 1.0$, $\Psi_r = 2.64$; 3. $\bar{r}_p = 2$ μm, $\nu_\infty = 1.0$, $\Psi_r = 7.47$; 4. $\nu \to 0$.

where γ_e and $\bar{c}_e$ are the effective ratio of the specific heats and the (equilibrium) sound velocity of the mixture. When γ_e and $\bar{c}_{e\infty}$ are used in place of γ and $\bar{c}_\infty$, respectively, in the non-dimensional basic equations for the system, the equations become the same as those for an ordinary single (gas)-phase flow. For the single-phase flow, the shock stand-off distance Δ is a function of M and γ. When the ratio of specific heats γ is fixed, Δ decreases with increasing M, and becomes insensitive to M for $M \gg 1$. It is well known that

$$\Delta \propto (\gamma-1)/(\gamma+1) \quad \text{for } M \gg 1. \tag{27}$$

When the gas condition is fixed, then the shock stand-off distance Δ is a decreasing function of the particle loading ratio ν_∞, because γ_e and $\bar{c}_e$ are decreasing with increasing ν_∞. This leads to the conclusion that the shock stand-off distance is a

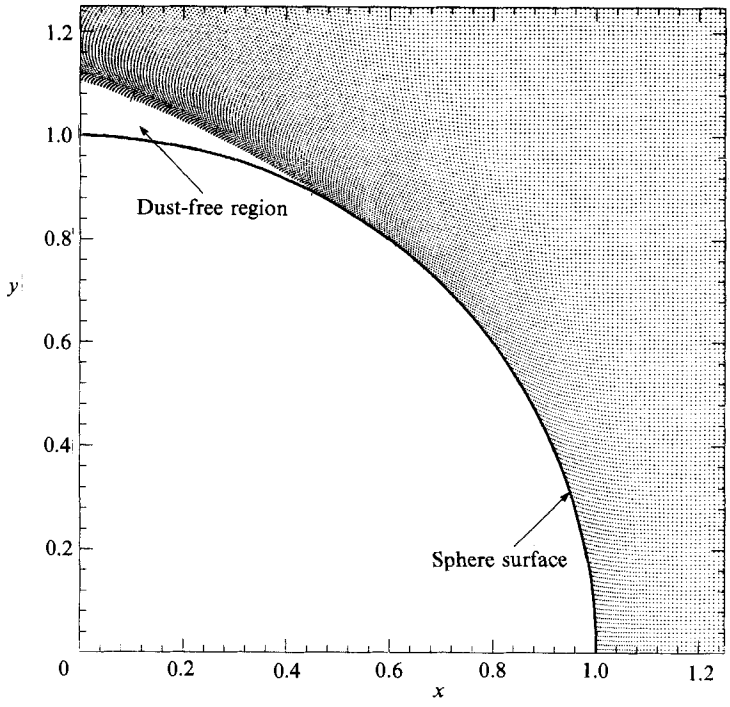

FIGURE 11. Locations of small particle clouds, $M_\infty = 3$, $\bar{p}_\infty = 0.5$ atm, $\bar{T}_\infty = 290$ K, $\bar{L} = 3$ cm, $\bar{r}_p = 1$ μm, $\nu_\infty = 0.3$, $\Psi_r = 1.93$, $n = 2200$.

decreasing function of ν. Since $\gamma_e \to 1$ as $\nu \to \infty$, then the shock stand-off distance is always very sensitive to ν for any Mach number M_e $(= \bar{u}_\infty/\bar{c}_e)$ at least in the equilibrium limit $(\Psi_r \to 0)$.

In order to investigate the particle behaviours in the shock layer, the spatial distributions of the small particle subclouds are shown in figures 11 and 12, where the number density of the subclouds considered in the actual calculations is reduced to one eighth. The particle trajectories in a dusty flow for a small Stokes number, which is slightly above the critical value, is shown in figure 13, where only a small number of trajectories are plotted to avoid confusion. Obviously, the grazing point is appreciably shifted in the upstream direction along the sphere surface. The concentration of the particle trajectories near this point is very strong, which is very similar to the theoretical prediction of Michael (1968) for the particle behaviour in an irrotational carrier gas around a sphere. Although a particle concentration is realized near the limiting particle streamline, especially in figure 13, it can be confirmed that there is no particle focusing. This situation is not dependent on the particle loading ratio ν. We may conclude that the intersection of particle streamlines does not occur in the supersonic two-phase flows around a sphere. The wavy pattern of particle trajectories near the body surface in figure 11 arises from the artificial disturbances included in the numerical solution.

Although. as was discussed previously, the structure of the dusty shock layer is strongly dependent on the particle loading ratio ν_∞, the particle trajectories are well correlated with the Stokes number Ψ_r. The collection factors E_p for the dusty flows obtained here are plotted against Ψ_r in figure 4 by solid circles. It is remarkable that these collection factors E_p are close to the correlation curve for $\nu_\infty \to 0$. With the increasing loading ratio ν_∞, the collection factor E_p is increased. This will mean that

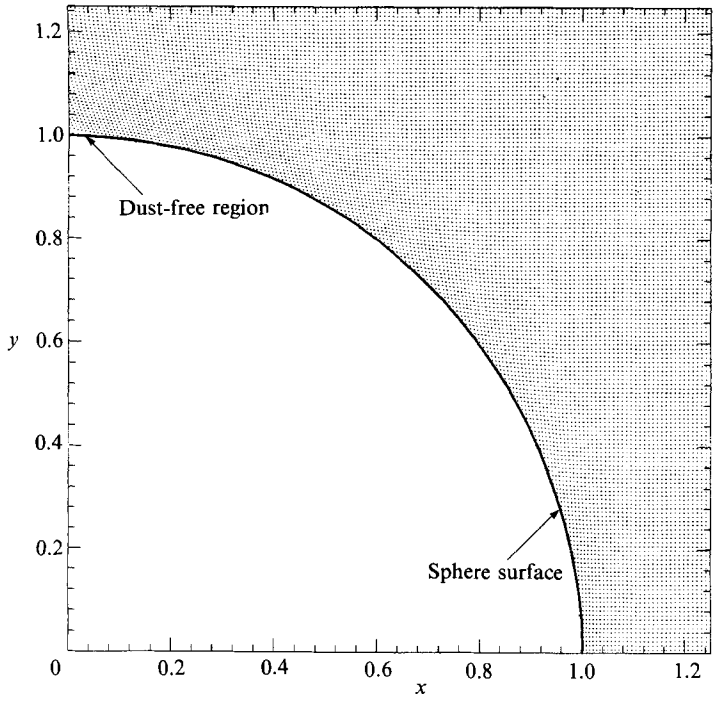

FIGURE 12. Locations of small particle clouds, $M_\infty = 3$, $\bar{p}_\infty = 0.5$ atm, $\bar{T}_\infty = 290$ K, $\bar{L} = 3$ cm, $\bar{r}_p = 2.0$ μm, $\nu_\infty = 5.0$, $\Psi_r = 7.94$, $n = 2200$.

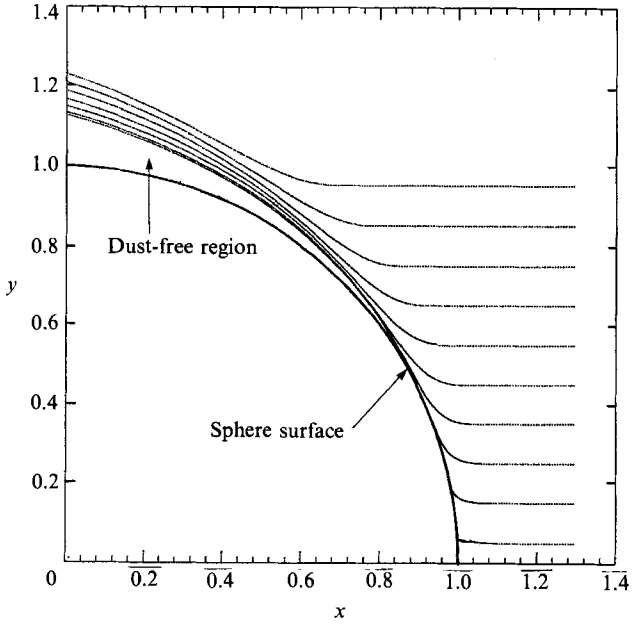

FIGURE 13. Particle streamlines for a small Stokes number, $M_\infty = 3$, $\bar{p}_\infty = 0.5$ atm, $\bar{T}_\infty = 290$ K, $\bar{L} = 3$ cm, $\bar{r}_p = 0.5$ μm, $\nu_\infty = 1.0$, $\Psi_r = 1.01$.

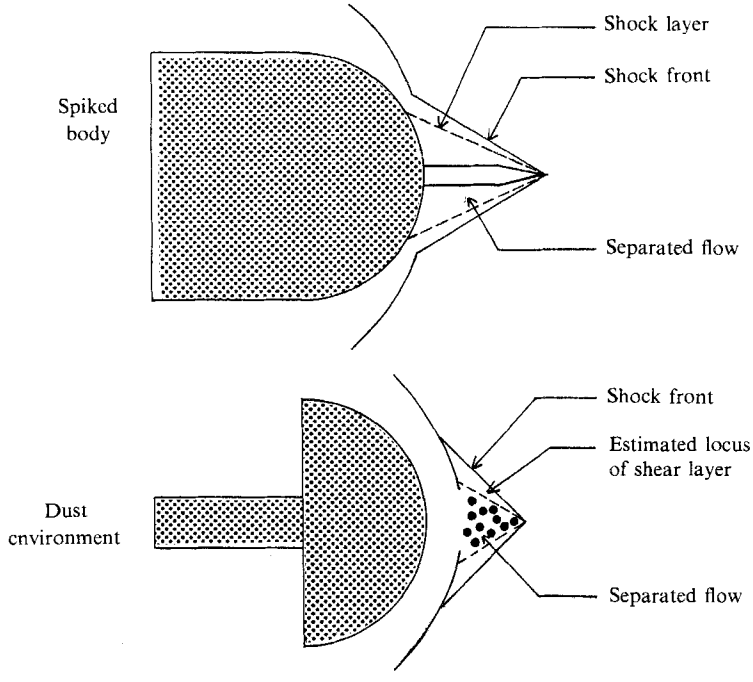

FIGURE 14. Comparison of dust- and spike-induced flow fields.

both E_p and $\Psi_r^{\frac{1}{2}}$ are increased roughly with the same rate by increasing the loading ratio ν_∞. In other words, the ratio $E_p/\Psi_r^{\frac{1}{2}}$ does not depend much on the loading ratio ν_∞.

So far very little has been known on the effects of the mass loading ratio ν_∞ on particle inertial effects. Recently, Park & Rosner (1989) have reported combined inertial and thermophoretic effects on the collection factor E_p in highly loaded dusty-gas sytems, where it is assumed that the fluid flow is incompressible and the Reynolds number is very small. However, because of the significant difference of the flow conditions, direct comparison of the present results with their results will be not appropriate.

4.4. *Unsteady two-phase flows*

In the early 1970s, a series of experimental tests was carried out to evaluate the performance of some metals (titanium, stainless steel, etc.) in an erosive hypersonic environment (Dunber *et al.* 1975; Fleener & Watson 1973). Measurements of heat transfer rates in these environments indicated heating levels far in excess of clean air values. These results were believed to be related to rebounded particles and surface debris interaction with the shock layer. In the high-speed motion pictures, rebounded dust particles were seen to produce intermittent conical perturbations of the bow shock. It has been postulated that the observed dust-induced flow structure is similar to that associated with spiked bodies. A comparison between the observed flow geometries for a spiked hemisphere and for a dust environment is made in figure 14. The flow field for a spiked body is characterized by separation of the spike boundary layer which results in a conical shock shape. In the dust case, it has been hypothesized that the wakes of rebounding particles provide a path for upstream communication of the shock-layer pressure, producing a conical separated region and the observed conical shock.

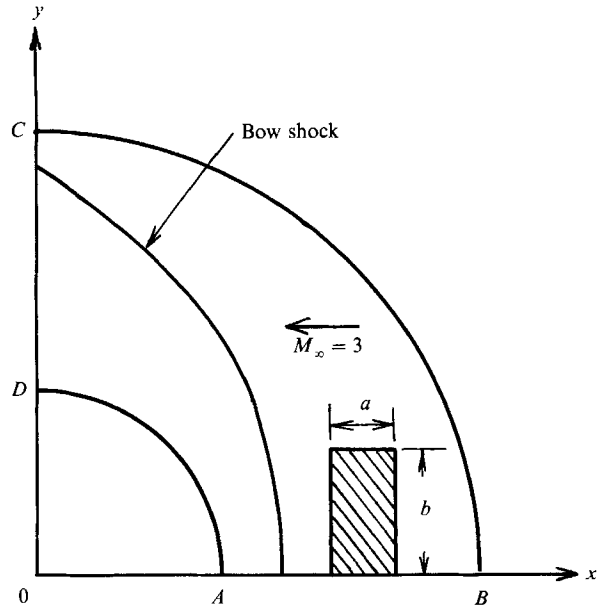

FIGURE 15. Particle cloud. At first, particles are present in a shaded disk region ahead of the bow shock, which has a thickness $a = 0.3$ and a radius $b = 0.2$, and this cloud is divided into 300×200 subclouds.

Here, unsteady flows over a sphere in a dust environment are simulated and the role played by the rebounded particles in the shock distortion is investigated. In the previous steady solutions, a case was treated where incident particles on the sphere are absorbed by the surface (perfectly inelastic reflection). When we try to calculate a steady-state dusty solution under the condition that the impinged particles are reflected elastically from the body surface, both the incident and reflected particles must simultaneously be traced in the flow field until a time-converged flow field is obtained. Since the rebounded particles remain in the flow field for a very long time, this requires a very large computer memory, far in excess of the capacity of our computer, and also requires a large amount of computing time. For these reasons the steady dusty flow in the elastic reflection case could not be treated in §4.3.

In the present unsteady calculations, there is no difficulty with the limited capacity of the computer resources. We consider two extreme cases: one is the case where the particles impinging on the sphere are reflected perfectly elastically (specular reflection) and the other is the case where they are reflected perfectly inelastically. By comparing these two results, it will be concluded that the rebounded particles play an important role in the distortion of the flow field when a large particle cloud impinges on a shock layer.

A steady supersonic flow at Mach number $M_\infty = 3$ of a dust-free gas around a sphere is given as the initial flow condition. As shown in figure 15, initially the particles are located only in the shaded rectangular region (a particle cloud) ahead of the bow shock. They are assumed to have the same local velocities and temperatures as those of the gas. The loading ratio of particles ν_∞ is set to 5.0. The axial and radial widths of the incident particle cloud are 0.3 and 0.2, respectively. This cloud is divided into 300×200 small subclouds.

First, we present the results obtained on the assumption of perfectly elastic reflection of the impinged particles on the sphere. The flow field of the gas and the

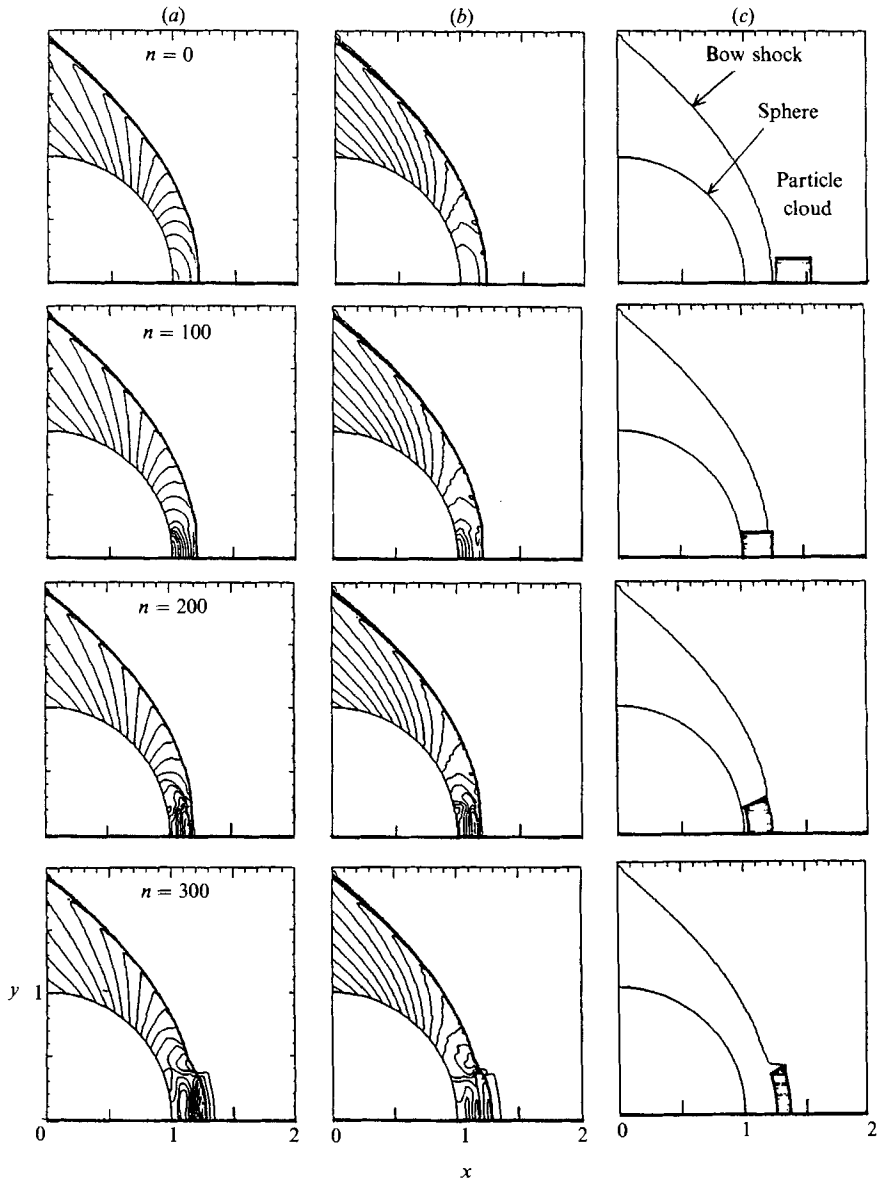

FIGURE 16. For caption see page 476.

configuration of the particle cloud are shown in figure 16 at every 100 timesteps for $n \leqslant 700$ and at every 300 timesteps for $n \geqslant 900$. It should be noted that each time interval $\Delta t = t^{n+1} - t^n$, where n is the integration timestep, is determined by the CFL (Coulant–Friedrichs–Lewy) condition for the gas-phase flow at $t = t^n$. Therefore it is not constant but dependent on the temporal gas condition (say a function of time t). Fortunately, however, in the present calculation, it was confirmed that the relation between the time t and the timestep n is regarded as nearly linear and $\Delta n = 100$ corresponds to $\Delta t\ (= \Delta \bar{t}/\bar{\tau}_{\mathrm{F}}) \approx 0.1$.

As the particles enter the shock layer, they push the gas towards the sphere and then the pressure waves are produced in front of the left-hand side of the particle cloud. These pressure waves reach the sphere at $t \approx 0.07$ and thereafter the particles

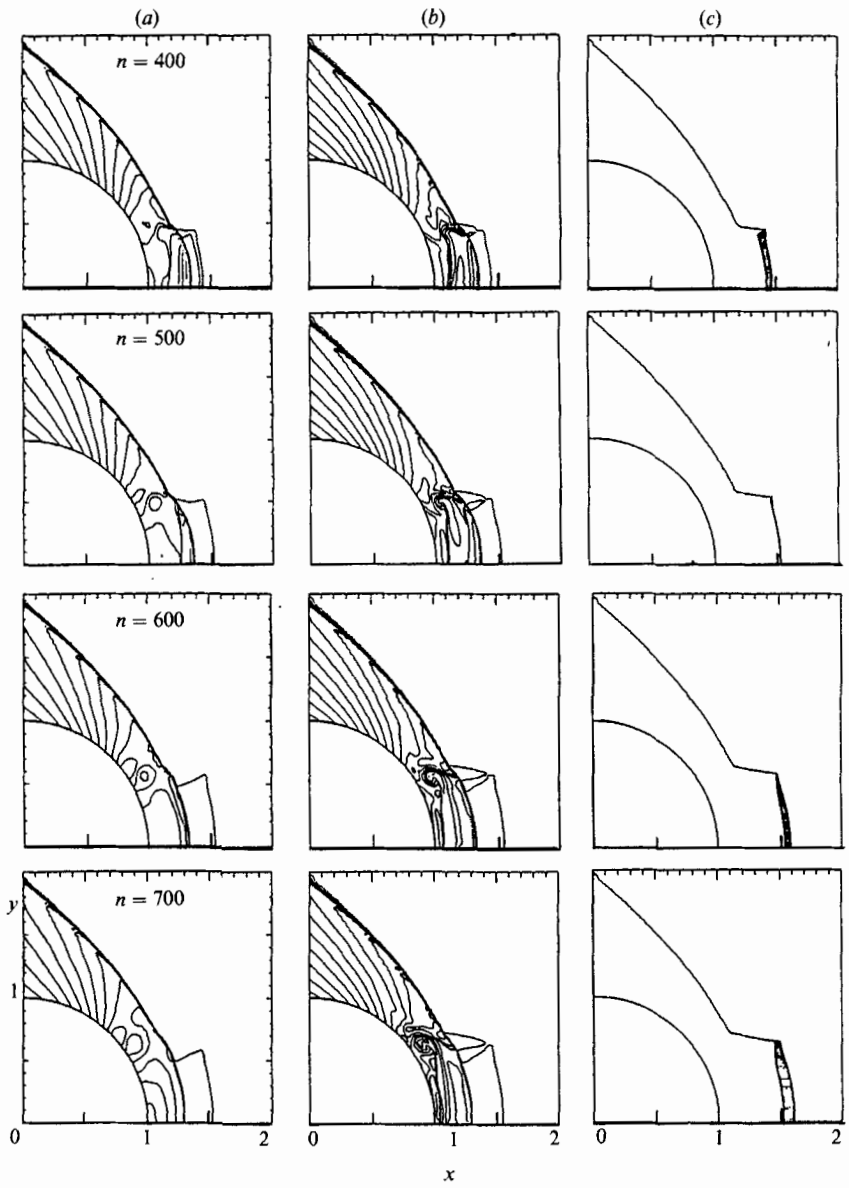

FIGURE 16. For caption see next page.

reach the sphere at $t \approx 0.1$, at which the highest density and pressure of the gas are attained at the stagnation point. By $t \approx 0.2$, all the particles complete their reflection from the sphere surface and the particles first impinged on and reflected from the surface reach the bow shock at $t \approx 0.2$. During this period, the shock stand-off distance continues to decrease and it attains the smallest value at $t \approx 0.2$.

On arriving at the bow shock, the reflected particle cloud pulls the gas and thereby the bow shock moves towards the upstream direction. After the reflection of the particle cloud, the gas near the stagnation point begins to expand rapidly like an 'explosion'. At $t \approx 0.2$, the gas velocity in this region becomes positive and a vortical structure (a ring vortex) is produced, which is convected downstream rather slowly along the body surface with time (see figure 18). In accordance with the vortex

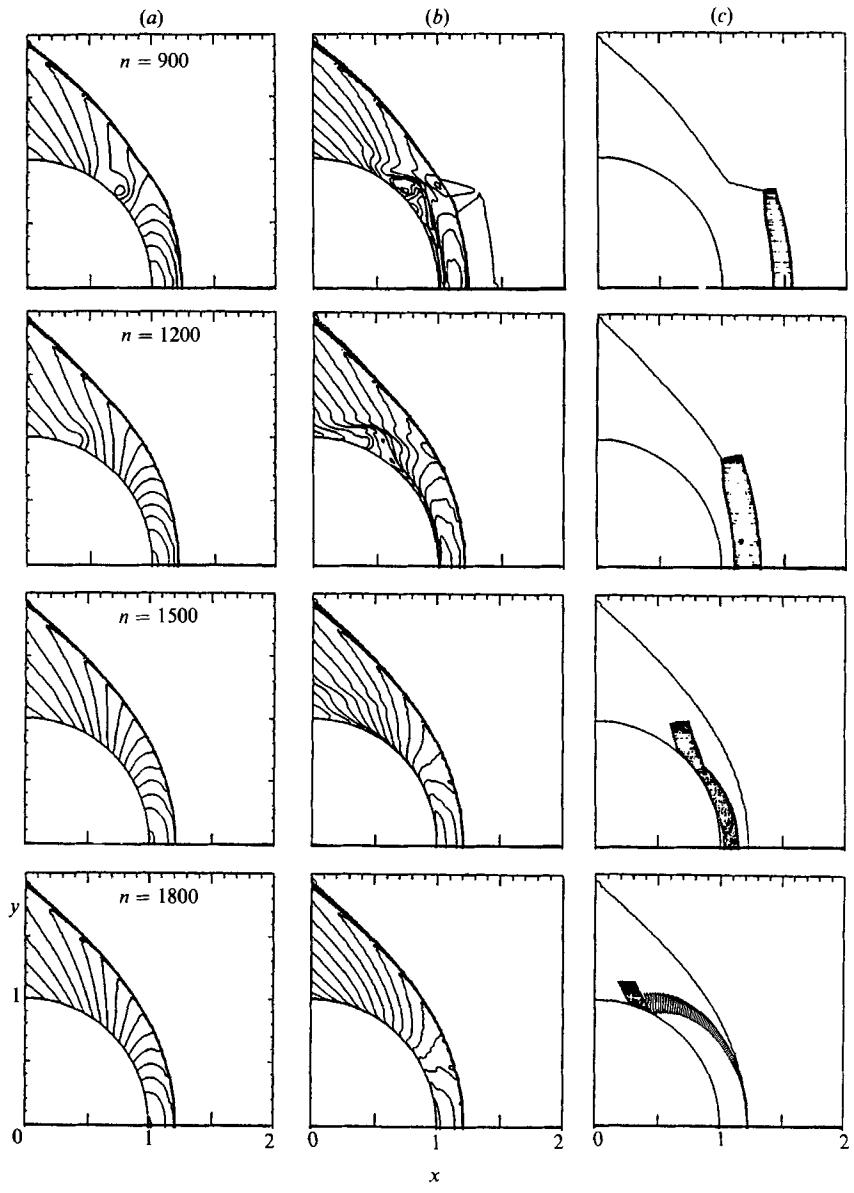

FIGURE 16. Flow field in front of the sphere for perfectly elastic reflection: (*a*) contours of constant pressure; (*b*) contours of constant density; (*c*) configuration of particle cloud.

generation, there appears a region where the pressure gradient along the surface is negative. This region moves downstream along the surface together with the vortex. Such a situation is clearly seen in figure 20(*a*), where the bottom of valley on the pressure curves nearly coincides with the instantaneous centre of the vortex.

At $t \approx 0.2$, some part of the particles pass through the bow shock and they are decelerated very rapidly owing to the strong frictional force exerted on them by the mainflow gas. The axial width of the particle cloud begins to decrease appreciably with time. At $t \approx 0.5$, the bow shock is distorted in the most remarkable state. The shock distortion in this stage is quite consistent with that observed in the previous experiments (Dunber *et al.* 1975). At the right-hand front of the particle cloud, a

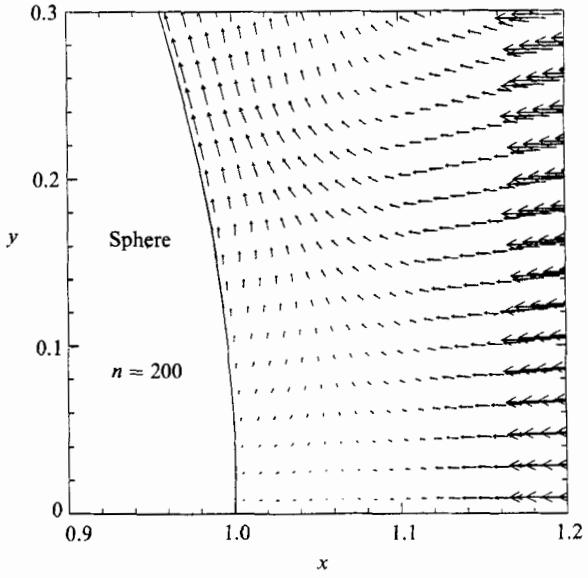

FIGURE 17. Velocity vectors at $t \approx 0.2$. A contact surface is formed between the outgoing and the incoming gases almost along the vertical line at an intermediate point in the shock layer.

weak shock wave is produced. Since the uniform flow is supersonic, this shock wave moves with the same speed as that of the right-hand front of the cloud. The particle cloud completely flows out of the shock layer by $t \approx 0.4$. The particles in the cloud still have positive axial velocity components which are different in the particles in the left-hand and the right-hand parts of the cloud. The particle velocities in the left-hand part are larger than those in the right-hand part. As a result, the particle cloud shrinks to a very thin disk. The thinnest disk is attained at $t \approx 0.5$, after which the disk width begins to increase again. Some particles reach the farthest point at $t \approx 0.7$. Since the reflected particles also have the radial velocity components, the disk radius is elongated to about three times its original value at $t \approx 0.7$. For $t > 0.7$, all the particles are pushed back towards the downstream direction owing to the drag force by the mainstream gas and then the particle cloud impinges again on the shock layer at $t \approx 1.3$.

It can be seen that the radial extent where the bow shock is appreciably distorted is increased in proportion to the increasing rate of the disk radius. When the particle cloud reimpinges on the shock layer at $t \approx 1.3$, the cross-sectional area of the cloud is about 13 times as large as its initial one and the averaged particle loading ratio over the cloud is about 0.4. For $t > 1.0$, the unsteady distortion of the bow shock is relatively small.

Just when the particle cloud is completely reflected, the highly compressed gas near the stagnation region begins to expand towards the upstream direction owing to the higher pressure beyond the ambient pressure and also owing to the frictional force exerted on the gas by the rebounded particles. The front of the expanding gas meets the gas coming in through the bow shock at an intermediate point between the sphere and the bow shock, where the flow directions of both gases are deflected nearly perpendicularly to the axis. From there, they proceed towards the radial direction to form a contact surface and also to generate a vortical structure. This situation is well demonstrated in figure 17. The vortical structure thus produced near the outer edge of the impinged cloud is convected downstream along the sphere. The centre of the

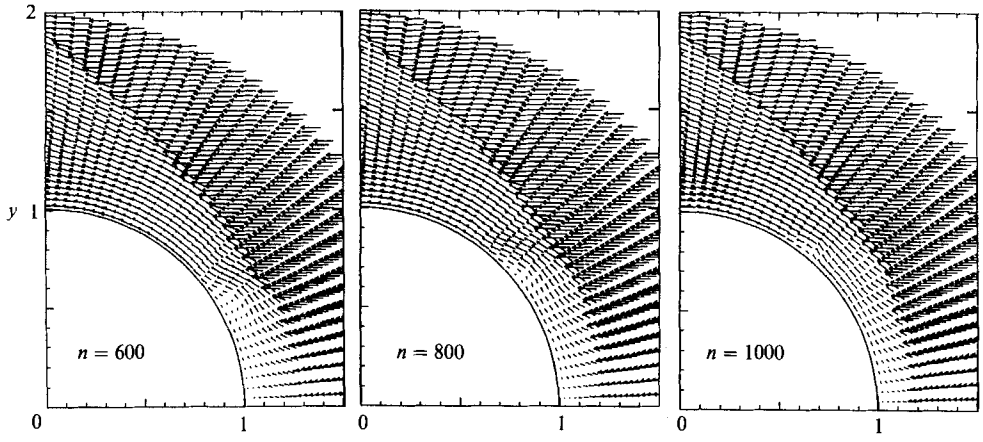

FIGURE 18. Velocity vectors at $t \approx 0.6$, 0.8 and 1.0.

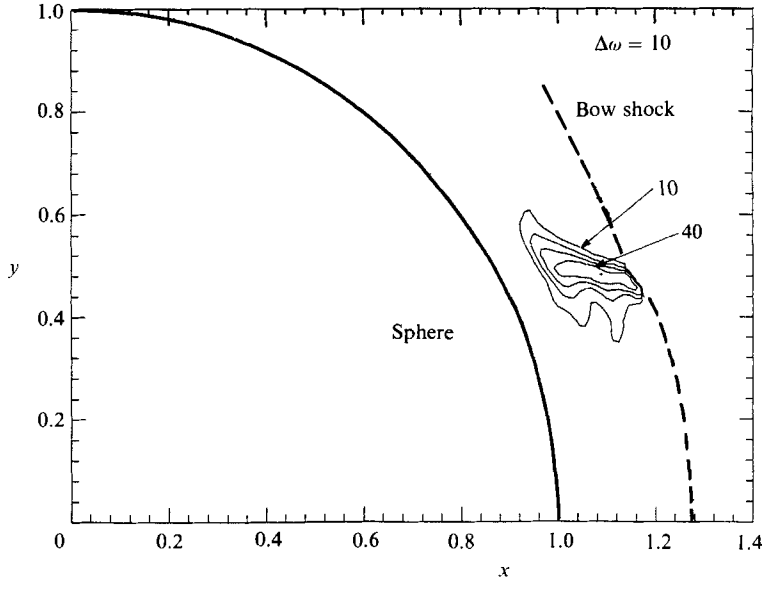

FIGURE 19. Vorticity ω of the gas flow in the shock layer at $t \approx 0.6$.

vortical structure can be recognized as a circular spot in the contours of the constant pressure or the constant density. In order to confirm these situations in more detail, the velocity vectors of the gas are shown in figure 18 for $t \approx 0.6$, 0.8 and 1.0. Figure 19 shows a distribution of vorticity ω,

$$\omega = \frac{1}{\xi}\frac{\partial}{\partial \xi}(\xi V_\eta) - \frac{1}{\xi}\frac{\partial V_\xi}{\partial \eta} \tag{28}$$

of the gas flow in the shock layer at $t \approx 0.6$, where V_ξ and V_η are the velocity components of the gas in the ξ- and η-directions. As shown in this figure, the centre of the vortex is at first located near the outer edge of the particle cloud. From figures 18 and 19, the presence of the vortical structure and its convection by the gas flow are well observed.

As seen in the contours of the constant density (figure 16), the contact surface (surface dividing the hot gas cloud produced by the particle impingement and the gas coming in through the distorted bow shock) first produced at $t \approx 2.0$ is always linked with the convecting vortical structure. Even after the vortical structure flows away from the computational domain, the contact surface remains near the body surface, which reuslts in the density field taking the longest time to regain its original dust-free one.

Here it must be noted that the particle cloud at $t \approx 0.5$ does not seem to satisfy one of the assumptions introduced in the present analysis, that is, the diluteness of the particles. In the present analysis, the volume fraction ϵ_p is obtained from

$$\epsilon_p = \frac{\nu_\infty}{\Gamma_\rho} \frac{1}{S_p} \sum N_{pk}, \tag{29}$$

where S_p is the averaging area and N_{pk} is the number of particles per unit length of the k-subcloud (Ishii *et al.* 1989).

In the most severe case at $t \approx 0.5$, the disk thickness is about 0.01 and the disk radius is about 0.8. This suggests that the average particle density $\bar{n}_p \bar{m}_p$ over the cloud is about 30 kg/m^3. This corresponds to a volume fraction ϵ_p of about 0.7×10^{-2}. This figure will, however, be sufficient for the assumption of diluteness of the particles. For example Matveyef & Seyukova (1981) proposed a correction of the particle drag coefficient for a finite volume fraction ϵ_p in the form,

$$C'_D = C_D(1 + 2.5\epsilon_p + 70\epsilon_p^2), \tag{30}$$

where C'_D is the modified particle drag coefficient. From this, one has $C'_D/C_D = 1.02$ for $\epsilon_p = 0.007$, and therefore it can be concluded that the error of C_D introduced by neglecting the volume fraction will be at most a few per cent, even in the most severe situation in the present results.

Figure 20 shows the time history of the pressure profile along the body surface. The profile is plotted at every 10 timesteps ($\Delta t \approx 0.01$). At first sight, it can be seen that the flow distortion induced by the particles is very significant and complicated. In this case, the reflected particles penetrate the bow shock and enter the uniform flow region. The particles interact with the gas flow in such a way as to produce an unsteady shock wave propagating upstream in front of the bow shock (see figure 16). The locus of this shock nearly coincides not with the particle path but with the focal line (the line connecting the particles located on the upstream side of the particle cloud at each time) of the particle paths. As shown in figure 21, the location of the bow shock on the body axis is disturbed very strongly by the impingement of the particle cloud.

Next, the results for the perfectly inelastic reflection of the particles will be mentioned. Figure 20 (*b*) shows the time history of the pressure profile along the body surface. In this case, the unsteady flow behaviour before the first impingement of the particles at the left-hand side of the cloud is the same as that in the previous elastic reflection case.

It is important to point out that the maximum pressure experienced by the gas at the stagnation point is higher in the perfectly inelastic reflection case than in the perfectly elastic reflection case.

Contours of the constant pressure, density of the gas and the *configuration of the* particle cloud are shown in figure 22 at every 100 timesteps for $0 \leqslant n \leqslant 300$. The difference between the results in the perfectly elastic and inelastic reflection cases are

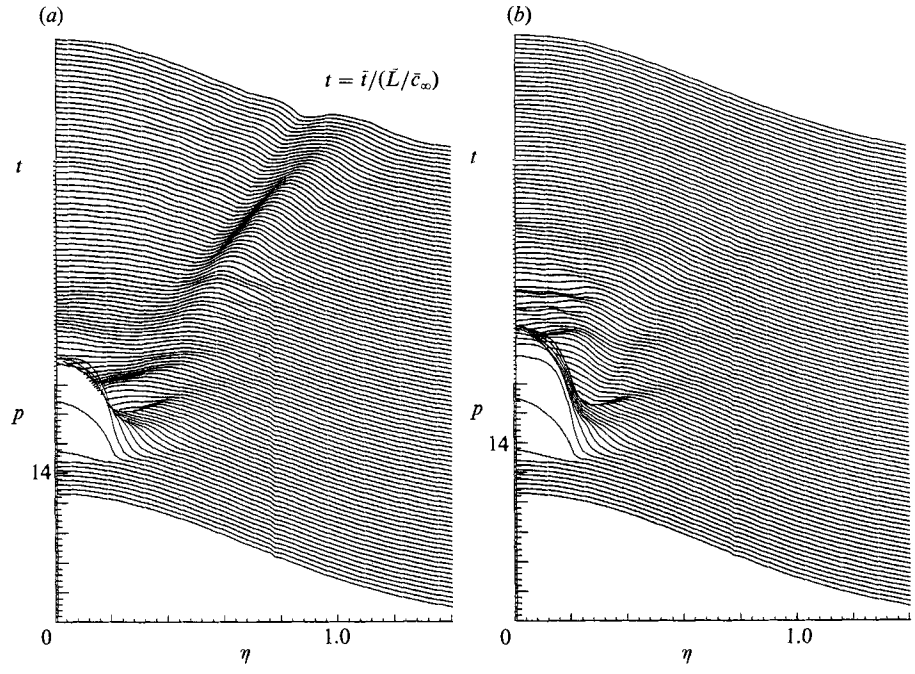

FIGURE 20. Time history of pressure profile along the body surface, $\bar{p}_\infty = 0.1$ atm, $\bar{T}_\infty = 290$ K, $M_\infty = 3$, $\bar{r}_p = 2.0$ μm, $\nu_\infty = 5.0$, $\bar{L} = 3$ cm: (*a*) perfectly elastic reflection; (*b*) perfectly inelastic reflection.

first seen at $t \approx 0.2$. After the reflection of the particle cloud, a vortical structure as well as a contact surface is induced. The growing mechanisms of the contact surface and the vortical structure are essentially the same as those in the previous case except for the absence of the frictional force exerted on the gas by the reflected particles. In the present case, however, the strength of the induced vortex is very much weaker than in the elastic reflection case. The vortex is convected by the gas along the surface, being linked with the terminal end of the contact surface, which is elongated with time and pushed closer and closer to the body surface.

By the impingement of the particle cloud on the shock layer, the shock stand-off distance is first decreased. Since the particles are removed from the flow field as soon as they impinge on the sphere, the bow shock regains its original location and shape relatively faster. Also the shock distortion is much smaller than in the elastic reflection case.

The vorticity produced in the flow field by the particle cloud is relatively much weaker than in the completely elastic reflection case. When it is shown in the same scale as in figure 19 at $t \approx 0.6$, any contours do not appear. This is because the magnitude of the vorticity ω is less than 10 in the whole computational domain in the completely inelastic reflection case.

By comparing the reuslts in figures 20 and 21, it can be concluded that the significant conical distortion of the bow shock observed in the previous experiments (Dunber *et al.* 1975) will not be produced by the impinging particles only or without the rebounded particles. The reflected particles play very important roles in the shock distortion and in the production of the vortical structure. The vortical stucture produced near the body axis is, however, partly different from that postulated in connection with the experimental observations (see figure 14).

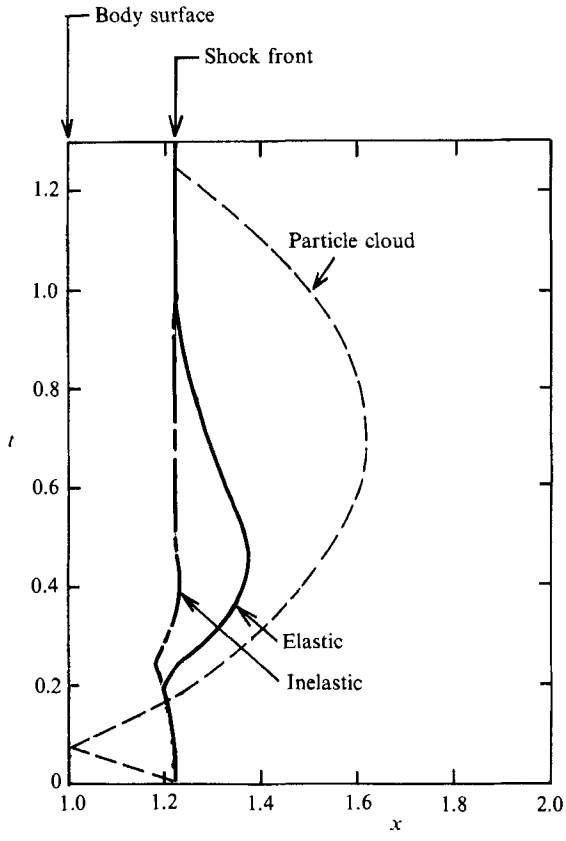

FIGURE 21. Variation of shock stand-off distance with time, $\bar{p}_\infty = 0.1$ atm, $\bar{T}_\infty = 290$ K, $M_\infty = 3$, $\bar{r}_p = 2.0$ μm, $\nu_\infty = 5.0$, $\bar{L} = 3$ cm. ——, shock stand-off distance; – – –, location of the front edge of the particle cloud.

5. Conclusion

Supersonic two-phase flows around a sphere were simulated numerically. It was found that an appreciable particle concentration can appear near the limiting particle streamline for the Stokes number of order unity. It is quite remarkable that the ratio of the collection factor E_p to the modified Stokes number $\Psi_T^{\frac{1}{2}}$ depends little on the particle mass loading ratio ν_∞.

When a large particle cloud impinges on a dust-free shock layer around a sphere, the flow field is significantly distorted and a reverse flow region is temporarily induced near the stagnation region. This reverse flow grows into a vortex. Then the flow model proposed previously to explain the experiments is partly supported by the present simulation. The vortical structure is always linked with a contact surface. The distortion of the bow shock is much stronger in the elastic reflection case than in the inelastic reflection one. This suggests that the rebounded particles play an important role in the distortion of the flow field around a blunt body. They may cause a strong separation of the gas flow near the body axis.

The authors whould like to express their cordial thanks to Professor D. Lhuillier for his valuable discussions and criticisms and also acknowledge support through a grant-in-aid for Scientific Research (C-01550532) of the Ministry of Education, Science and Culture in Japan.

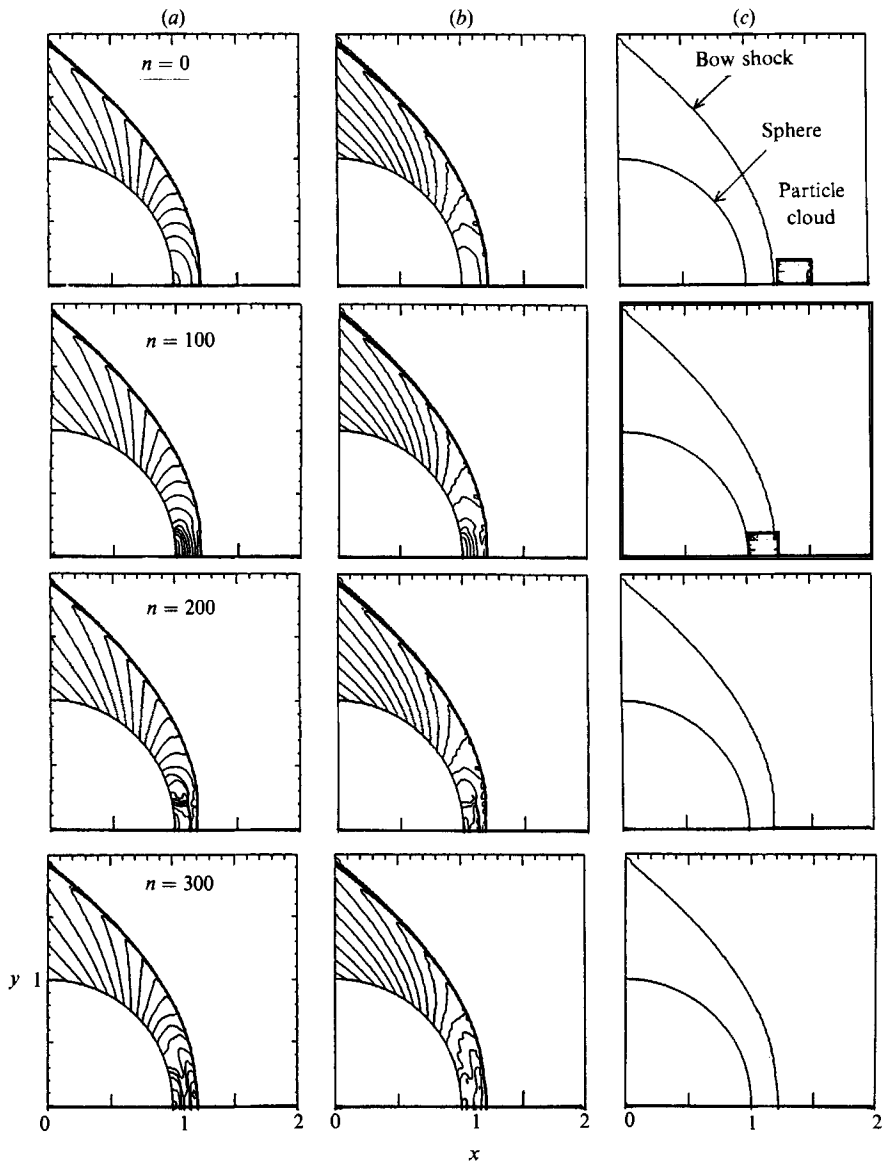

FIGURE 22. Flow field in the shock layer for perfectly elastic reflection: (*a*) contours of constant pressure; (*b*) contours of constant density; (*c*) configuration of particle cloud.

REFERENCES

BATCHELOR, G. K. 1988 A new theory of the instability of a uniform fluidized bed. *J. Fluid Mech.* **193**, 75–110.

BATCHELOR, G. K. 1989 A brief guide to two-phase flow. In *Theoretical Applied Mechanics* (ed. G. Germain, M. Piau & D. Caillerie), pp. 27–56. Elsevier.

BELOTSERKOVSKII, O. M. 1960 The calculation of flows past axisymmetric bodies with detached shock waves. *J. Appl. Maths Mech.* **24**, 744–753.

CARLSON, D. J. & HOGLUND, R. F. 1973 Particle drag and heat transfer in rocket nozzles. *AIAA J.* **11**, 1980–1984.

CHAKRAVARTHY, S. R. & OSHER, S. 1985 A new class of high accuracy TVD schemes for hyperbolic conservation laws. *AIAA paper* 85-0363.

CHUNG, J. N. & TROUTT, T. R. 1988 Simulation of particle dispersion in an axisymmetric jet. *J. Fluid Mech.* **186**, 199–222.

DUNBER, L. E., COURTNEY, J. F. & MCMILLEN, L. D. 1975 Heating augmentation in erosive hypersonic environments. *AIAA J.* **13**, 908–912.

FERNÁNDEZ DE LA MORA, J. & RIESCO-CHUECA, P. 1988 Aerodynamic focusing of particles in a carrier gas. *J. Fluid Mech.* **198**, 1–21.

FERNÁNDEZ DE LA MORA, J. & ROSNER, D. E. 1982 Effects of inertia on the diffusional deposition of small particles to spheres and cylinders at low Reynolds numbers. *J. Fluid Mech.* **125**, 379–395.

FLEENER, W. A. & WATSON, R. H. 1973 Convective heating in dust-laden hypersonic flow. *AIAA paper* 73-761.

FORNEY, L. J. & MCGREGOR, W. K. 1987 Particle sampling in supersonic streams with a thin-walled cylindrical probe. *AIAA J.* **25**, 1100–1104.

GILBERT, M., DAVIS, L. & ALTMAN, D. 1955 Velocity lag of particle in linearly accelerated combustion gases. *Jet Prop.* **25**, 26–30.

GODUNOV, S. K. 1959 A finite difference method for the numerical solutions of the equations of fluid dynamics. *Mat. Sb.* **47**, 271–306.

HENDERSON, C. B. 1976 Drag coefficient of spheres in continuum and rarefied flows. *AIAA J.* **14**, 707–708.

ISHII, R. 1983 Shock waves in gas–particle mixtures. *Mem. Fac. Engng Kyoto Univ.* XLV-3, 1–16.

ISHII, R., UMEDA, Y. & YUHI, M. 1989 Numerical analysis of gas–particle two-phase flow. *J. Fluid Mech.* **203**, 475–515.

ISRAEL, R. & ROSNER, D. E. 1983 Use of a generalized Stokes number to determine the aerodynamic capture efficiency of non-Stokesian particles from a compressible gas flow. *Aerosol. Sci. Tech.* **2**, 45–51.

LHUILLIER, D. 1986 Mass and entropy transport in a suspension of rigid particles. *J. Phys. Paris* **47**, 1687–1696.

MARBLE, F. F. 1970 Dynamics of dusty gases. *Ann. Rev. Fluid Mech.* **2**, 397–446.

MATSUDA, T., UMEDA, Y., ISHII, R., YASUDA, A. & SAWADA, K. 1987 Numerical and experimental studies on choked underexpanded jets. *AIAA paper* 87-1378.

MATVEYEF, S. K. & SEYUKOVA, L. P. 1981 Calculation of the flow of a dust-laden gas over a disk and flat end of a cylinder. *Fluid Mech. Sov. Res.* **10**, 1–8.

MICHAEL, D. H. 1968 The steady motion of a sphere in a dusty gas. *J. Fluid Mech.* **31**, 175–192.

MORIOKA, S. & NAKAJIMA, T. 1987 Modeling of gas and particle two-phase flow and application to fluidized bed. *J. Theor. Appl. Mech.* **6**, 77–88.

PARK, H. M. & ROSNER, D. E. 1989 Combined inertial and thermophoretic effects on particle deposition rates in highly loaded dusty-gas systems. *Chem. Engng Sci.* **44**, 2233–2244.

ROBINSON, A. 1956 On the motion of small particles in a potential field of flow. *Commun. Pure Appl. Maths* **9**, 69–84.

VAN DYKE, M. D. 1958 A model of supersonic flow past blunt axisymmetric bodies, with application of Chester's solution. *J. Fluid Mech.* **3**, 515–522.